Operando spectral imaging of the lithium ion battery's solid-electrolyte interphase

Jared J. Lodico*[1,2], Matthew Mecklenburg*[2,3], Ho Leung Chan[1,2], Yueyun Chen[1,2], Xin Yi Ling[1], and B. C. Regan†[1,2]

[1] *Department of Physics and Astronomy, University of California, Los Angeles, CA 90095, U.S.A.*
[2] *California NanoSystems Institute, University of California, Los Angeles, CA 90095, U.S.A.*
[3] *Core Center of Excellence in Nano Imaging, University of Southern California, Los Angeles, California, 90089, U.S.A.*

May 5, 2023

Abstract

The lithium-ion battery is currently the preferred power source for applications ranging from smart phones to electric vehicles. Imaging the chemical reactions governing its function as they happen, with nanoscale spatial resolution and chemical specificity, is a long-standing open problem. Here we demonstrate *operando* spectrum imaging of a Li-ion battery anode over multiple charge-discharge cycles using electron energy-loss spectroscopy (EELS) in a scanning transmission electron microscope (STEM). Employing ultra-thin Li-ion cells, we acquire reference EELS spectra for the various constituents of the solid-electrolyte interphase (SEI) layer and then apply these 'chemical fingerprints' to high-resolution, real-space mapping of the corresponding physical structures. We observe the growth of Li and LiH dendrites in the SEI and fingerprint the SEI itself. High spatial- and spectral-resolution *operando* imaging of the air-sensitive liquid chemistries of the Li-ion cell opens a direct route to understanding the complex, dynamic mechanisms that impact battery safety, capacity, and lifetime.

Introduction

The lithium ion battery (LIB), already the most common rechargeable battery, also constitutes the fastest growing market segment [1]. Given its enormous economic importance, it is perhaps surprising that basic questions remain about the chemistry governing the operation of the LIB. Ideally, charging and discharging a Li-ion cell simply moves Li^+ ions back and forth between the cell's graphite anode and its metal-oxide cathode as an equal number of electrons travel separately through the external circuit. However, many important and poorly understood side reactions occur as well [2–6]. In particular, a fragile and multi-component structure forms at the electrode-electrolyte interface during the first few charge-discharge cycles that plays a key role in preserving the electrode's chemical and structural integrity over the hundreds of cycles that follow [2–4, 7–10]. This solid-electrolyte interphase (SEI) layer has been famously referred to as the most important and least understood component of the LIB [3, 11].

In situ and *operando* techniques are invaluable for gaining understanding of the SEI: its structural evolution, chemical composition, and functional behavior [12, 13]. X-ray [14, 15], electron [13], neutron [16], magnetic resonance [17], optical [18, 19], and scanning probe [20–22] imaging and/or spectroscopy provide complementary insights into realistic Li-ion cells. Of these characterization techniques, electron microscopy, particularly transmission electron microscopy (TEM), offers a unique combination of superlative spatial resolution and spectroscopic chemical identification; traditionally its main drawback has been the difficulties associated with applying it to the beam-sensitive, room-temperature, liquid electrolytes used in practical batteries [12, 13].

High-resolution characterization of realistic lithium-ion battery (LIB) chemistries is extremely challenging [8, 10, 21, 23–28]. LIB sample preparation for high resolution imaging with (S)TEM has previously involved invasive procedures that alter, or have the potential to alter, the structural and

*These authors contributed equally.
†regan@physics.ucla.edu

chemical integrity of the interface regions. Examples include freezing the sample [29–31], washing [32] and/or drying it [29, 31, 33, 34], or milling it with a focused ion beam [28, 30]. Furthermore, with the liquid electrolytes used by most LIBs, these approaches [29–31,33,34] provide only a static snapshot of the sample. *In situ* imaging of LIB chemistries has been demonstrated using commercially available and homemade TEM liquid cells [23–27]. However, the cells are so thick (typically $\gtrsim$ 500 nm) that image and spectral quality, especially at core-loss energy scales, is severely degraded [23, 35]. In fact, core-loss EELS of lithium in liquid-cell TEM has been described as "practically impossible" [23].

Results

Using first an argon atmosphere and then vacuum to avoid air exposure, we assemble ultra-thin, sealed electrochemical fluid cells that allow high-quality STEM EELS imaging of realistic Li-ion battery chemistries under *operando* conditions. Two silicon chips framing 20 nm-thick Si_3N_4 windows form the body of the TEM-compatible fluid cell (Fig. 1A). The bottom chip is instrumented with four platinum leads.

To assemble the cell, a single-crystal flake of natural graphite [1, 36], which serves as the anode (the negative electrode), is first mechanically exfoliated from bulk graphite and fixed to one of the platinum leads [37]. A $\lesssim$ 10 pL droplet of 1M $LiClO_4$ in ethylene carbonate:dimethyl carbonate (EC:DMC) is then deposited on the graphite electrode in an argon atmosphere, which protects the air-sensitive electrolyte [36, 38]. The top chip is aligned and sealed to the bottom chip with epoxy, first under 1 atm of argon and then finally under rough vacuum (Figs. 1B, 1C, S1), which maintains the moisture-free environment while minimizing the pressure differential that develops across the membrane windows when the fluid cell is placed in the electron microscope's high vacuum. If the fluid cell is sufficiently clean and thin, surface tension brings the membrane windows together during assembly, making them concave-in. Sealing the fluid cell under vacuum allows the cell to remain concave-in in the microscope's high vacuum, unlike commercial set-ups, which are generally concave-out [39]. The final, vacuum-assembly step, which is directly analogous to the final vacuum-sealing step in commercial lithium-ion pouch manufacturing, is essential to achieving a thin ($\lesssim$ 50 nm thick) liquid layer and correspondingly good STEM imaging conditions (Figs. S4–S5).

To examine the SEI formation, we bias a fluid cell *in situ* through two lithiations (i.e. charging half-cycles) while acquiring EELS spectrum images of the graphite-electrolyte interface. During the first lithiation, we scan an area (red box in Fig. 1D) containing the left edge of the graphite flake. The electron beam rasters from left to right (fast scan direction) and then top to bottom (slow scan direction) across the imaged area. During the second lithiation we similarly scan an area containing the right edge of the graphite (yellow box in Fig. 1D). The substantial overlap between the two imaged regions serves as a control, in that it reveals the extent to which imaging with the electron beam modifies the electrode. In both regions the graphite thickness is not uniform: beyond the easily visible 'bulk edge' lies an extended region of thinner few-layer graphite (i.e. multilayer graphene) that terminates at the 'true edge' (Fig. S3).

ADF STEM images acquired in parallel with the EELS spectrum images provide structural information that can be related to the electrochemical transport data (Fig. 2). The transport data (Figs. 2A,D) is oriented and scaled such that its time axis aligns with the vertical axis (i.e. the slow scan direction) of the corresponding ADF image (Figs. 2B,C,E,F). Lithium intercalation 'events' [37], where variously-sized groups of lithium ions are abruptly inserted between the graphene layers, give rise to electrical current pulses. These events are associated with structural changes, e.g. AB-to-AA stacking changes, in the graphite that produce contrast changes in the ADF STEM images. Because these structural reconfigurations can occur on timescales much shorter than the row-scanning time of the electron beam, the associated contrast changes often appear as horizontal stripes in the ADF STEM images [37].

The first cycle begins with the pristine, unlithiated graphite working electrode (WE) at its open-

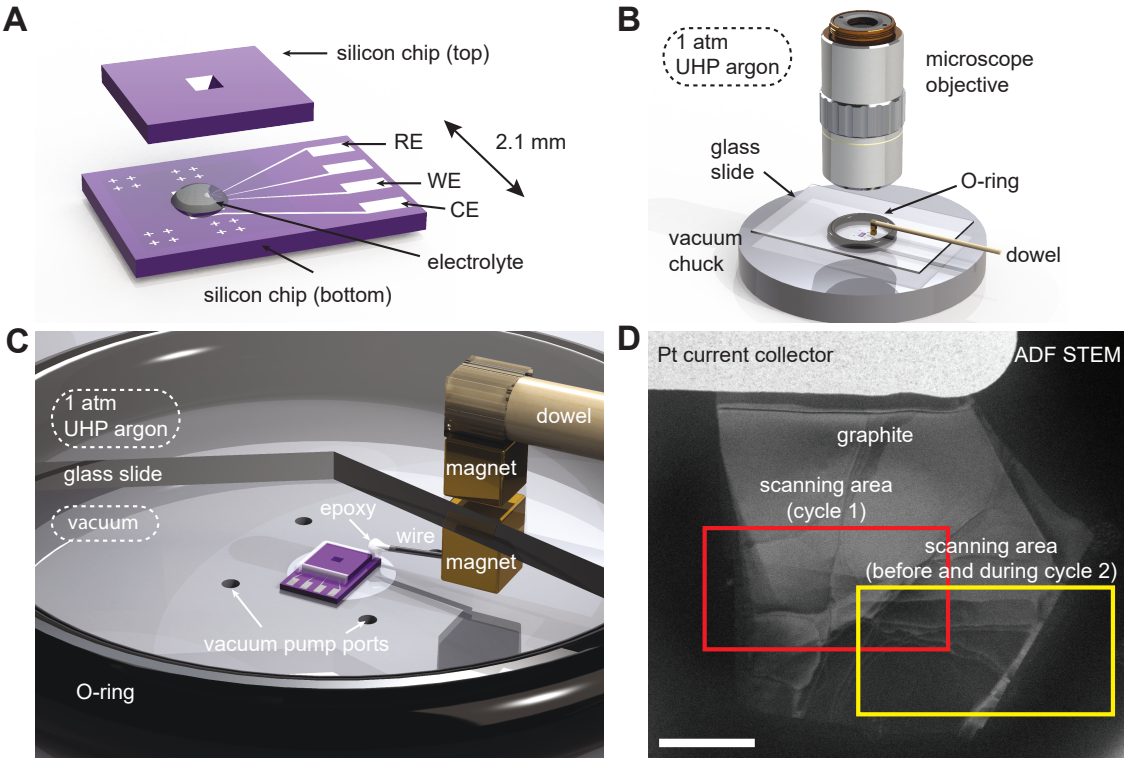

Figure 1: **Liquid cell imaging platform for STEM EELS. (A)** Schematic showing an exploded view of the fluid cell. A droplet of 1M $LiClO_4$ in EC:DMC serves as the electrolyte and as the lithium source (Fig. S2). The top and bottom chips are epoxied together on three sides in a glove bag under 1 atm of ultra-high-purity argon. **(B)** The fourth and final edge is sealed inside a vacuum chamber assembled inside the glove bag (not shown). **(C)** A zoom view with a cutaway in the glass slide shows how opposing NdFeB magnets provide mechanical access for epoxying inside the vacuum chamber (Fig. S1). **(D)** ADF STEM image of a pristine graphite flake contacted by a platinum electrode within a sealed fluid cell. Red and yellow boxes outline the scan areas for the first and second lithiations, respectively. The scale bar is 2 μm.

circuit potential of −1.86 V relative to the Pt pseudo-reference electrode. As the electrode potential is ramped at −2 mV/s, lithium ions begin intercalating the graphite, as indicated by the non-zero current (Fig. 2A). To prevent overcharging, once the current magnitude exceeds 200 pA we switch to manual control of the electrode potential. At −3 V, a large current peak appears in the electrical transport data. Simultaneously, the graphite exhibits flake-wide ADF contrast changes (Fig. 2B) indicative of massive structural changes associated with intercalation [37]. Shortly thereafter several features abruptly emerge outside the graphite along the true edge (Fig. 2C).

The second lithiation is much like the first. Early in the potential ramp, the intercalation current (Fig. 2D) is small and regular. The current becomes larger and more irregular slightly before −3.0 V, and the intercalation current pulses are associated with abrupt, flake-wide contrast changes (i.e. the horizontal streaks) in the simultaneously acquired ADF STEM image (Fig. 2E). Later in the intercalation, the graphite assumes a disordered appearance in the ADF STEM image that is qualitatively different from that seen in the first lithiation. This difference between the first and the second lithiations mirrors results obtained with optical microscopy: the first lithiation irreversibly changes the graphite so as to make subsequent intercalations much more disorderly [36].

The EELS spectrum images add, literally, a whole new dimension to the picture provided by the transport data and the ADF STEM imaging. Converting the spectrum images to a time-series of energy-filtered images (Movie S1), we see distinct areas light up in various energy windows; the features grown off the graphite's true edge are not as chemically homogeneous as ADF imaging alone would indicate. (Because the movie format conflates energy and time, the spectrum image movies S1 and S4 are best viewed in a player with a progress bar that can be dragged to specific energies.) Based on their low-loss spectral signatures, we identify two of the most prominent constituents as lithium [25,30,40,41] and lithium hydride [30]. Lithium has a signature plasmon peak at 7.5 eV. Lithium hydride has a plasmon peak at 15.1 eV with a shoulder near 12.2 eV [42] due to the hydrogen core loss signal [30]. Averaging over regions-of-interest (ROIs) with the strong characteristic signals, we define representative spectra for these materials, as well as for the un-intercalated graphite, the membranes-plus-electrolyte, and a third material that we will refer to as the SEI (Figs. 2G, S6).

These representative spectra define a basis for multiple linear least squares (MLLS) fitting [28,43,44] of the entire spectrum image. We choose MLLS because, compared to other common algorithms [45], it is easier to implement and interpret. Applying MLLS to the Fig. 2 dataset gives composition maps of the graphite flake as it undergoes these first two lithiations. Both lithiations show Li and LiH dendrites growing adjacent to the graphite late in the charging period (Figs. 2C,F), and in both lithiations the dendrite growth is preceded by similar current pulses and associated changes in the ADF contrast of the graphite flake.

To confirm the chemical identifications, we turn from the low-loss part of the spectrum to examine the Li core-loss signal (Fig. 3). During the first lithiation, as one proceeds from top-to-bottom in real space along the graphite's edge (which also corresponds to advancing in time, as explained above), a diffuse signal in the 50–80 eV bandwidth is consistently increasing from zero. Spectra acquired from each of the first seven ROIs indicated on the map show quantitatively that this signal is specifically increasing near the Li K-edge at 55 eV (Fig. 3D). With the 8^{th} ROI this spectral signal jumps up abruptly right at the K-edge, indicating the appearance of lithium metal. The 9^{th} and 10^{th} ROIs also show strong Li signals, but with a chemical shift (about 2 eV) and fine structure indicative of LiH [30]. The 11^{th} ROI is like the 8^{th} ROI, indicating lithium metal again. These composition identifications based on the Li core-loss signals alone (Fig. 3) are thus entirely consistent with the identifications made based on the low-loss signals alone (Fig. 2).

After the first lithiation the graphite electrode's potential is ramped at 2 mV/s from −3.05 V to 0 V and disconnected. The spectrum image acquired in this condition (Fig. 3B) shows a diffuse lithium core-loss signal all along the graphite edge (Fig. 3D, gray curves #12–22). The individual ROIs all exhibit a

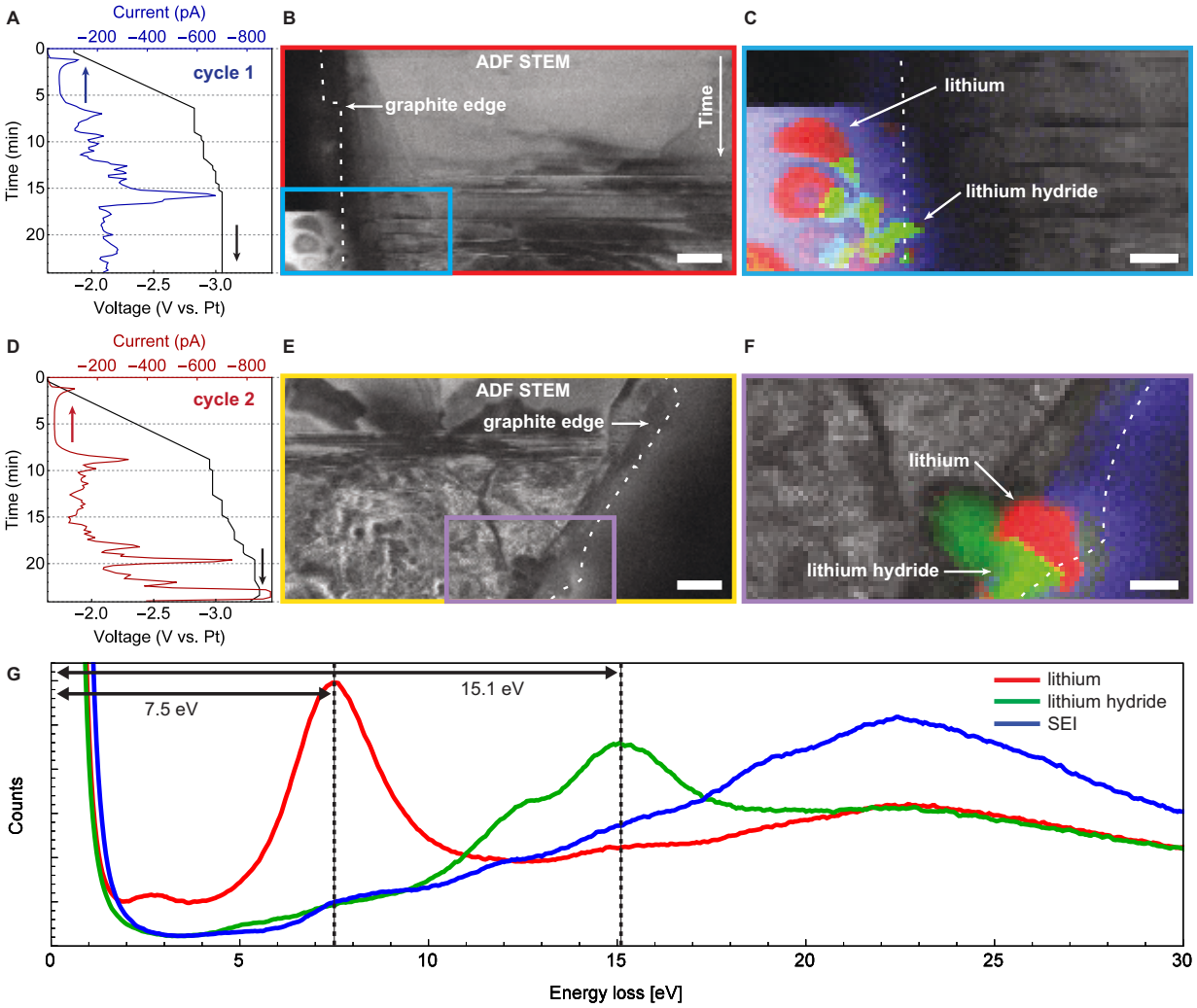

Figure 2: **Lithiating a single crystal graphite flake.** White dashed lines indicate the graphite's true edge (Fig. S3). The measured current data from the first lithiation **(A)** is aligned and averaged so that each time point represents a single row of pixels in **(B)** the simultaneously-acquired ADF STEM image. **(C)** A zoom view of the region indicated in (B), with red, green, and blue overlays on the ADF STEM image that indicate the presence of Li, LiH, and SEI, respectively, as determined by MLLS fitting (Fig. S6). **(D–F)** The corresponding data for lithiation 2. **(G)** Low-loss EELS spectra of lithium metal (red), lithium hydride (green), and the solid-electrolyte interphase (blue). The scale bars are 500 nm in (B, E) and 200 nm in (C, F).

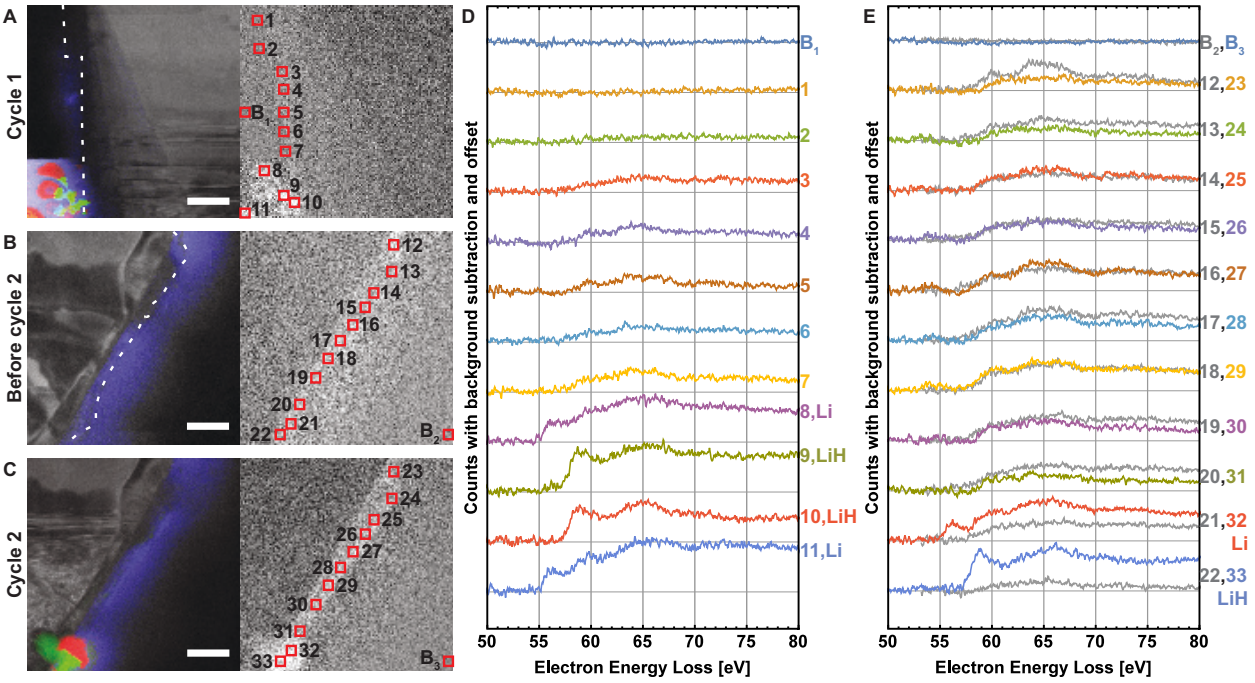

Figure 3: **Chemical evolution at the solid-liquid interface during lithiation.** ADF STEM images of the graphite flake with MLLS color overlays (see Fig. 2) **(A)** during the first lithiation, **(B)** before cycle 2, and **(C)** during lithiation 2 (left) and the corresponding, energy-filtered maps of the EELS intensity integrated over 50–80 eV, after background subtraction (right). We emphasize that, once the reference spectra are chosen, the MLLS mapping is entirely automated over the whole field of view. **(D, E)** Background-subtracted spectra summed over the regions indicated by red boxes in (A–C). Each box is 5×5 pixels, which corresponds to 107 nm$\times$107 nm. The scale bar is 500 nm in (A–C).

Li signal, but generally with a chemical shift that is perhaps larger than that of LiH. Thus while the graphite has returned to the uncharged state, the edge of the electrode has not returned to its pristine condition. This diffuse lithium core-loss signal represents an irreversible capacity loss that originates from the SEI that forms during the first lithiation and persists thereafter [3, 5–7], as we will return to discuss shortly.

During the second lithiation, the diffuse lithium signal in the early ROIs #23–31 does not develop further, indicating that the SEI is roughly unchanging. On the other hand, the late ROIs #32 and #33 show spectra indicating the appearance of Li and LiH, respectively. Again, the core-loss spectra present a consistent picture with the low-loss spectra: both show Li and LiH dendrites appearing at the end of the lithiation, when the potential is lowest, and in the same locations.

The data of Figs. 2–3 are acquired with a beam current of 75 pA, a probe full-width at half maximum of 0.7 nm, and a pixel size of 21 nm (Table S1). Thus with a dwell time of 50 ms the effective fluence (often colloquially referred to as 'dose' [46]) per spectrum image can be quantified as $6 \times 10^5\, e/\text{Å}^2$ or $500\, e/\text{Å}^2$, depending on whether the relevant averaging area is taken to be the beam area or the pixel area, respectively [46, 47]. Although this distinction is not always made [30] (or the fluence is not reported at all [25,33]), the spectrum acquired in a given spectrum image reflects the damage implied by the larger fluence number.

Regardless, repeated STEM imaging with these dose conditions does not significantly impact the electrode, either in how the anode absorbs electrical charge or in how the graphite/lithium structure evolves morphologically. The transport data for the first two lithiations is very similar, and the boundaries of the thrice-imaged (Figs. 2–3) control area can barely be distinguished (see also the delithiation Movies S2 and S3). Put another way, lithiation and delithiation — the processes under study — have a far greater effect on the graphite electrode [36] than the STEM spectrum imaging. Viewed together, Figs. 2–3 and Movies S1–S3 demonstrate that this electrochemical cell can be cycled multiple times, without appreciable degradation of the electrode due to the imaging electron beam, and with enough EELS signal to robustly locate and identify the Li and LiH species of dendrite in both low-loss and core-loss spectra. Compared to the electrode, however, the SEI is not robust in the electron beam (Figs. S9–S12, Movie S4).

To acquire a more detailed spatial and spectroscopic picture of the SEI, we produce a complete SEI layer that is denser and more developed by twice ramping a second LIB cell from its open-circuit potential in the pristine state to −5.7 V and back. This aggressive cycling generates dendrites, some gas evolution, and the desired SEI. ADF STEM imaging shows a variety of dendritic features adjacent to the graphite edge (Fig. 4A), but the morphology of these features alone is insufficiently informative to allow for chemical identification [30]. Viewed with ADF imaging (Fig. 4A), the SEI appears to be relatively uniform and barely distinguishable from the electrolyte.

Spectrum imaging in a 0–90 eV bandwidth (Table S1) allows us to map the SEI with chemical specificity and nanoscale spatial resolution. We again apply MLLS (Figs. 4B–E, S7), this time using seven reference spectra: four acquired from the spectrum image itself (Li, LiH, graphite, and background) and three measured previously [48] (Li_2O, Li_2CO_3, and LiOH). The combination of EELS spectrum imaging and MLLS analysis reveals what ADF imaging does not: the layer decorating the graphite edge is a chemically heterogeneous.

This layer (Fig. 4B) consists of lithium, lithium hydride, and a diffuse 'SEI' (Fig. 4E) that surrounds the Li and LiH. This 'extended' SEI is $\sim$ 500 nm wide, and unlikely to survive any sample preparation involving washing [30]. The Li and LiH, both rich in low-Z lithium, generate less scattering into the dark field than the background electrolyte and SEI, and they thus appear dark in the ADF image. Both the Li and the LiH are near but not directly adjacent to the graphite electrode. These dendrites are disconnected near their attachment points [27, 30, 49] during the delithiation process and represent partially inactive or completely inactive (i.e. 'dead') lithium that does not have a metallic connection to the electrode [9,26,

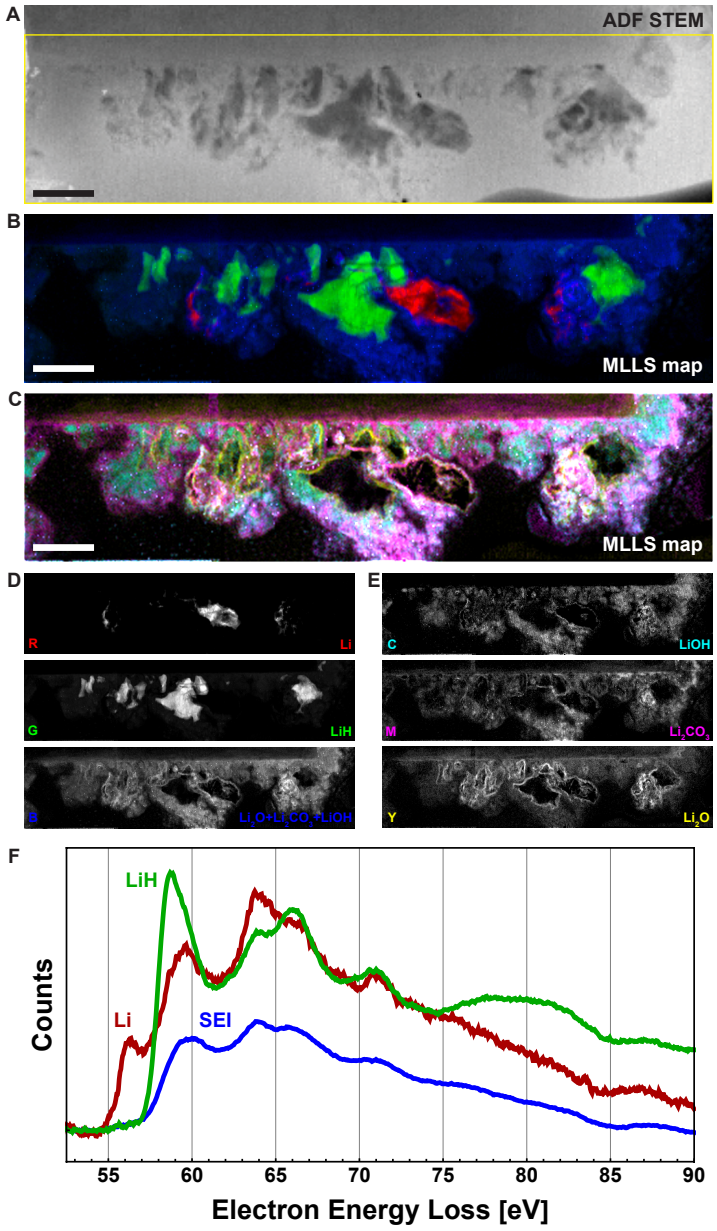

Figure 4: **Denser, more developed SEI. (A)** ADF STEM survey image of a graphite electrode with an SEI formed by two complete lithiation-delithiation cycles *in situ*. The graphite occupies a rectangular region extending from the upper left corner across 90% of the top edge. **(B)** Red, green, and blue (RGB) and **(C)** cyan, magenta, yellow (CMY) MLLS composite images (see Methods) based on a 102.4 eV bandwidth spectrum image with field of view indicated by the yellow box in (A). **(D, E)** Corresponding grayscale MLLS images showing the individual components of (B, C), respectively (Fig. S7). The scale bars are 500 nm. **(F)** Background-subtracted Li core-loss signals found by calculating intensity-weighted averages over the maps (D).

30].

This MLLS decomposition shows lithium carbonate and lithium hydroxide with similar, but not identical, spatial distributions throughout the SEI. The combination image 'Li_2O+Li_2CO_3+LiOH' (Fig. 4D), the sum of the three listed components (Fig. 4E), shows the SEI with the same spatial extent as that found by choosing a reference spectrum from a representative SEI region in the spectrum image (Fig. S9). The strong, well-resolved lithium oxide signal in a thin layer surrounding the LiH and Li dendrites indicates that the dendrites have a oxide shell that is $\lesssim$ 10-nm thick. Of course, MLLS decomposition only reveals compounds represented in the reference spectra basis. Lithium hydroxide monohydrate and any number of lithium alkyl carbonates are likely present but unidentified, as their fingerprints are not included. Future studies would benefit greatly from the creation of an extended library of low-loss EELS reference spectra for SEI compounds.

The Li, LiH, and SEI have enough areal density to give high-quality Li core-loss spectra (Fig. 4F). These spectra, with their superior signal-to-noise ratio and well-resolved near-edge fine structure and chemical shifts [28–30, 33], are in excellent agreement with those of Figs. 3D,E. Because the lithium carbonate and hydroxide signals are essentially co-located, independent core-loss spectra for these materials cannot be determined from these data. However, these ultrathin liquid cells provide such good spectroscopic access that, with a comprehensive set of reference spectra, one could apply MLLS also to the Li core-loss data [28] and thereby obtain time-resolved chemical identification of the SEI that is independent of, and complementary to, the low-loss fingerprinting.

Discussion

The complexity of the SEI's composition, structure, and formation dynamics is fully evident in our data. Under *operando* conditions and thus without invasive sample processing, we see an SEI that ranges from 10's to 100's of nanometers thick, depending on the charging conditions [2, 4, 30, 33]. We see no remarkable differences in the structure of the SEI surrounding Li dendrites vs. that surrounding LiH dendrites [30]. The SEI that we observe has a composition that is fully consistent with that proposed by the well-known 'mosaic' model [4, 6]. On the other hand, excepting the dendrites and their oxide shells (which are not necessary nor desirable components of an SEI), we see no structures that can fairly be described as being akin to the tiles of a mosaic. Although, for instance, the relative concentrations of Li_2O and Li_2CO_3 vary throughout the SEI, with our nanometer-scale spatial resolution we see no evidence for abrupt 'grain boundaries' between microphases [5, 6]. Pressed to give an analogy, we would say that the SEI appears to be more like pastry dough, where incomplete mixing of flour, water, salt, sugar, and fat produces a structure that is not homogeneous, but not as well segregated as a mosaic either.

In conclusion, we observe a chemically heterogeneous SEI that consists primarily of inorganic Li compounds, as has been seen previously using other methods [4–6]. However, *operando* STEM EELS allows this interfacial layer to be observed, as it grows, with a combination of spatial resolution and chemical identification that is unmatched by other techniques. We clearly see, for instance, not only Li and LiH dendrites, but also their nanometer-scale oxide shells. Unfortunately, however, here we are only able to detect and map the SEI compounds that qualify as well-known suspects. This shortcoming is not fundamental. Expanded libraries of EELS fingerprints would allow these methods to provide a more complete picture of the form and function of the SEI, without adding experimental complexity.

Materials and Methods

Fluid cell fabrication:

Silicon sample-biasing chips with 20-nm-thick, 15 μm $\times$ 70 μm electron-transparent Si_3N_4 windows and instrumented with Ti/Pt (5/25 nm) electrodes are microfabricated as described previously (Fig. 1A) [37]. Flakes of natural graphite (NGS Naturagraphit GmBH) are mechanically exfoliated from bulk with

adhesive tape and stamped onto a sacrificial Si/SiO_2 (500 μm/80 nm) wafer. Under an optical microscope, a flake with thickness in the desired 15–40 nm range is identified. Using the wet transfer method, this flake is then deposited on an electrode on a 'bottom' sample biasing chip [37].

To prevent electrochemistry on the Ti/Pt electrode from obscuring the graphite's electrochemical contribution to the electrical current, the entire chip is blanketed with a 20 nm conformal layer of aluminum oxide (Al_2O_3) via atomic layer deposition (ALD). Using a photoresist mask patterned with optical lithography and a buffered oxide etch (BOE), unwanted Al_2O_3 is removed from the contact pads outside the cell and from the graphite, the counter electrode (CE), and the reference electrode (RE).

The fluid cells are assembled and sealed at room temperature in a custom-built argon atmosphere glove bag. A ∼0.2 pL droplet of 1M lithium perchlorate ($LiClO_4$) in ethylene carbonate [$(CH_2O)_2CO$]: dimethyl carbonate [$OC(OCH_3)_2$] (EC:DMC) (v:v = 1:1) acts as the electrolyte and the lithium source. Color changes in a graphite flake (Fig. S2) demonstrate that lithium intercalates the graphite. These color changes [36] confirm that the electrolyte contains sufficient lithium to fully intercalate flakes of the sizes used in this study.

A second 'top' chip with a matching electron transparent Si_3N_4 window seals the fluid cell. Using micromanipulators, the 'top' chip is manually maneuvered above the 'bottom' chip with the graphite, electrodes, and electrolyte, until the electron-transparent windows of two chips are aligned. Three of the four edges are sealed under one atmosphere of argon with vacuum-compatible epoxy. To minimize the pressure differential present across the Si_3N_4 membranes when the cell is in the TEM, the fourth and final edge is sealed under house vacuum using the same epoxy (Figs. 1B, 1C, S1).

The thickness of the cells (Figs. S4–S5) is determined using EELS and the 'log-ratio' method [50].

STEM spectrum imaging and *in situ* biasing:

A Hummingbird Scientific biasing holder and a Gamry 600 potentiostat are used to electrically drive the fluid cells *in situ* while imaging them with STEM. All STEM images are acquired in a JEOL JEM-2100F at 200 kV accelerating voltage with a 80 mm STEM camera length. EELS spectra are acquired with a Gatan Quantum 963 spectrometer with a STEM beam convergence angle $\alpha = 9$ mrad and a spectrometer collection angle $\beta = 6$ mrad through a 2.5 mm aperture (or 12 mrad through a 5 mm aperture). We achieve a zero-loss peak with a full-width at half-maximum of 0.75 eV. Additional imaging parameters are given in Table S1. Buffered current and voltage output signals from the potentiostat are digitized and recorded synchronously with the STEM data, allowing for line-by-line correlation between the images and the electrical transport data.

Multiple linear least squares (MLLS) fitting:

To map the different chemical components (e.g. lithium, lithium hydride, graphite, the SEI, etc.) in the electrochemical fluid cells, multiple linear least-square (MLLS) regression is used to decompose the EELS spectrum at each beam position [28,43,44]. For each material, a representative (spatial) region of interest (ROI) is located in the spectrum image that is structurally and spectrally homogeneous. The EELS spectra inside this ROI are summed and then normalized such that the total intensity of the zero-loss peak (ZLP) is unity. This normalized, average spectrum is used as a reference spectrum for the MLLS fitting. In MLLS fitting the EELS spectrum at each beam position is decomposed into a best-fit linear combination of the reference spectra over a particular energy range. ('Best fit' is defined as the list of amplitudes that minimizes the squared deviations between the spectral decomposition and the actual spectrum.) We fit over 4–40 eV for Figs. 2–3 and over 5–25 eV for Fig. 4, with the range limited in the second case by the data available in Ref. [48]. The EELS spectra to be fit are normalized relative

to their ZLP in the same way as the reference spectra are, and the spectral amplitudes are constrained to be non-negative. The constraint is enforced by an iterative fit algorithm in Mathematica which, if a negative amplitude is detected, sets the amplitude of the corresponding reference spectrum to zero and re-fits until all of the best fit amplitudes are non-negative. Ideally the best fit amplitudes are then indicative of the amount of the corresponding material present at that STEM beam position. Repeating the MLLS procedure at each beam position thus generates a distribution map for each material.

Color coding and overlaying the MLLS distribution maps can produce a quantitative map showing how the different chemical constituents (e.g. lithium, lithium hydride, the SEI) are distributed relative to one another across the field of view. To create an RGB composite image of three SEI components, grayscale images of the individual SEI components are converted to red, blue, and green intensities and simply added. To create a CMY composite image of three SEI components, the grayscale images of the individual components are converted to cyan, magenta, and yellow images first. (Equal amounts of green and blue RGB value, red and blue RGB value, and red and green RGB value give rise to the cyan, magenta, and yellow colors respectively.) These individual images are then added together to produce a CMY composite image, which, unlike an RGB composite image, might be saturated in some areas. Despite this defect, we use CMY for Fig. 4C to avoid indicating different chemicals with the same color, and because the colors in RGB can be difficult to distinguish (RG) or see clearly on a black background (B).

Acknowledgments

This work was supported by National Science Foundation (NSF) Science and Technology Center (STC) award DMR-1548924 (STROBE) and by NSF awards DMR-1611036 and DMR-2004897. Silicon microfabrication was performed in the UCLA Nanolab and electron microscopy was performed at the USC Core Center of Excellence in Nano Imaging.

Author contributions: J.J.L., M.M., and B.C.R. conceived the idea and supervised the project. J.J.L. and M.M. designed the experiments. J.J.L. microfabricated and assembled the electrochemical fluid cells. J.J.L., M.M., and H.L.C. acquired the electrochemical and TEM data. M.M. developed the analysis for the EELS data. J.J.L., M.M., Y.C., and X.Y.L. did the data analysis. J.J.L. and B.C.R. wrote the paper with contributions from all of the authors.

Competing interests: The authors declare that they have no competing interests.

Data availability: All data needed to evaluate the conclusions in the paper are present in the paper and/or the Supplementary Materials.

References

[1] Pillot, C. The Rechargeable Battery Market and Main Trends 2016-2025. 98 (2017). 34th International Battery Seminar & Exhibit, Fort Lauderdale.

[2] Verma, P., Maire, P. & Novák, P. A review of the features and analyses of the solid electrolyte interphase in Li-ion batteries. *Electrochimica Acta* **55**, 6332–6341 (2010).

[3] Xu, K. Electrolytes and Interphases in Li-Ion Batteries and Beyond. *Chemical Reviews* **114**, 11503–11618 (2014).

[4] Gauthier, M., Carney, T. J., Grimaud, A., Giordano, L., Pour, N., Chang, H.-H., Fenning, D. P., Lux, S. F., Paschos, O., Bauer, C., Maglia, F., Lupart, S., Lamp, P. & Shao-Horn, Y. Electrode–Electrolyte Interface in Li-Ion Batteries: Current Understanding and New Insights. *The Journal of Physical Chemistry Letters* **6**, 4653–4672 (2015).

[5] An, S. J., Li, J., Daniel, C., Mohanty, D., Nagpure, S. & Wood, D. L. The state of understanding of the lithium-ion-battery graphite solid electrolyte interphase (SEI) and its relationship to formation cycling. *Carbon* **105**, 52–76 (2016).

[6] Peled, E. & Menkin, S. Review—SEI: Past, Present and Future. *Journal of The Electrochemical Society* **164**, A1703 (2017).

[7] Wang, A., Kadam, S., Li, H., Shi, S. & Qi, Y. Review on modeling of the anode solid electrolyte interphase (SEI) for lithium-ion batteries. *npj Computational Materials* **4**, 1–26 (2018).

[8] Wang, L., Menakath, A., Han, F., Wang, Y., Zavalij, P. Y., Gaskell, K. J., Borodin, O., Iuga, D., Brown, S. P., Wang, C., Xu, K. & Eichhorn, B. W. Identifying the components of the solid–electrolyte interphase in Li-ion batteries. *Nature Chemistry* **11**, 789–796 (2019).

[9] Tao, S., Li, M., Lyu, M., Ran, L., Wepf, R., Gentle, I. & Knibbe, R. In Operando Closed-cell Transmission Electron Microscopy for Rechargeable Battery Characterization: Scientific Breakthroughs and Practical Limitations. *Nano Energy* **96**, 107083 (2022).

[10] Liu, T., Lin, L., Bi, X., Tian, L., Yang, K., Liu, J., Li, M., Chen, Z., Lu, J., Amine, K., Xu, K. & Pan, F. In situ quantification of interphasial chemistry in Li-ion battery. *Nature Nanotechnology* **14**, 50–56 (2019).

[11] Winter, M. The Solid Electrolyte Interphase – The Most Important and the Least Understood Solid Electrolyte in Rechargeable Li Batteries. *Zeitschrift für Physikalische Chemie* **223**, 1395–1406 (2009).

[12] Liu, D., Shadike, Z., Lin, R., Qian, K., Li, H., Li, K., Wang, S., Yu, Q., Liu, M., Ganapathy, S., Qin, X., Yang, Q.-H., Wagemaker, M., Kang, F., Yang, X.-Q. & Li, B. Review of Recent Development of In Situ/Operando Characterization Techniques for Lithium Battery Research. *Advanced Materials* **31**, 1806620 (2019).

[13] Harks, P. P. R. M. L., Mulder, F. M. & Notten, P. H. L. In situ methods for Li-ion battery research: A review of recent developments. *Journal of Power Sources* **288**, 92–105 (2015).

[14] Bak, S.-M., Shadike, Z., Lin, R., Yu, X. & Yang, X.-Q. In situ/operando synchrotron-based X-ray techniques for lithium-ion battery research. *NPG Asia Materials* **10**, 563–580 (2018).

[15] Lim, J., Li, Y., Alsem, D. H., So, H., Lee, S. C., Bai, P., Cogswell, D. A., Liu, X., Jin, N., Yu, Y.-s., Salmon, N. J., Shapiro, D. A., Bazant, M. Z., Tyliszczak, T. & Chueh, W. C. Origin and hysteresis of lithium compositional spatiodynamics within battery primary particles. *Science* **353**, 566–571 (2016).

[16] Nazer, N. S., Strobl, M., Kaestner, A., Vie, P. J. S. & Yartys, V. A. Operando neutron imaging study of a commercial Li-ion battery at variable charge-discharge current densities. *Electrochimica Acta* **427**, 140793 (2022).

[17] Mohammadi, M. & Jerschow, A. In situ and operando magnetic resonance imaging of electrochemical cells: A perspective. *Journal of Magnetic Resonance* **308**, 106600 (2019).

[18] Chen, B., Zhang, H., Xuan, J., Offer, G. J. & Wang, H. Seeing is Believing: In Situ/Operando Optical Microscopy for Probing Electrochemical Energy Systems. *Advanced Materials Technologies* **5**, 2000555 (2020).

[19] Meyer, L., Saqib, N. & Porter, J. Review—Operando Optical Spectroscopy Studies of Batteries. *Journal of The Electrochemical Society* **168**, 090561 (2021).

[20] Cresce, A. v., Russell, S. M., Baker, D. R., Gaskell, K. J. & Xu, K. In Situ and Quantitative Characterization of Solid Electrolyte Interphases. *Nano Letters* **14**, 1405–1412 (2014).

[21] Zhang, Z., Smith, K., Jervis, R., Shearing, P. R., Miller, T. S. & Brett, D. J. L. Operando Electrochemical Atomic Force Microscopy of Solid–Electrolyte Interphase Formation on Graphite Anodes: The Evolution of SEI Morphology and Mechanical Properties. *ACS Applied Materials & Interfaces* **12**, 35132–35141 (2020).

[22] Legerstee, W. J., Boekel, M., Boonstra, S. & Kelder, E. M. Scanning Probe Microscopy Facility for Operando Study of Redox Processes on Lithium ion Battery Electrodes. *Frontiers in Chemistry* **9** (2021).

[23] Holtz, M. E., Yu, Y., Gunceler, D., Gao, J., Sundararaman, R., Schwarz, K. A., Arias, T. A., Abruña, H. D. & Muller, D. A. Nanoscale Imaging of Lithium Ion Distribution During In Situ Operation of Battery Electrode and Electrolyte. *Nano Letters* **14**, 1453–1459 (2014).

[24] Zeng, Z., Liang, W.-I., Liao, H.-G., Xin, H. L., Chu, Y.-H. & Zheng, H. Visualization of Electrode–Electrolyte Interfaces in LiPF6/EC/DEC Electrolyte for Lithium Ion Batteries via in Situ TEM. *Nano Letters* **14**, 1745–1750 (2014).

[25] Sacci, R. L., Black, J. M., Balke, N., Dudney, N. J., More, K. L. & Unocic, R. R. Nanoscale Imaging of Fundamental Li Battery Chemistry: Solid-Electrolyte Interphase Formation and Preferential Growth of Lithium Metal Nanoclusters. *Nano Letters* **15**, 2011–2018 (2015).

[26] Mehdi, B. L., Qian, J., Nasybulin, E., Park, C., Welch, D. A., Faller, R., Mehta, H., Henderson, W. A., Xu, W., Wang, C. M., Evans, J. E., Liu, J., Zhang, J. G., Mueller, K. T. & Browning, N. D. Observation and Quantification of Nanoscale Processes in Lithium Batteries by Operando Electrochemical (S)TEM. *Nano Letters* **15**, 2168–2173 (2015).

[27] Kushima, A., So, K. P., Su, C., Bai, P., Kuriyama, N., Maebashi, T., Fujiwara, Y., Bazant, M. Z. & Li, J. Liquid cell transmission electron microscopy observation of lithium metal growth and dissolution: Root growth, dead lithium and lithium flotsams. *Nano Energy* **32**, 271–279 (2017).

[28] Nomura, Y., Yamamoto, K., Fujii, M., Hirayama, T., Igaki, E. & Saitoh, K. Dynamic imaging of lithium in solid-state batteries by operando electron energy-loss spectroscopy with sparse coding. *Nature Communications* **11**, 2824 (2020).

[29] Li, Y., Li, Y., Pei, A., Yan, K., Sun, Y., Wu, C.-L., Joubert, L.-M., Chin, R., Koh, A. L., Yu, Y., Perrino, J., Butz, B., Chu, S. & Cui, Y. Atomic structure of sensitive battery materials and interfaces revealed by cryo–electron microscopy. *Science* **358**, 506–510 (2017).

[30] Zachman, M. J., Tu, Z., Choudhury, S., Archer, L. A. & Kourkoutis, L. F. Cryo-STEM mapping of solid–liquid interfaces and dendrites in lithium-metal batteries. *Nature* **560**, 345–349 (2018).

[31] Han, B., Zhang, Z., Zou, Y., Xu, K., Xu, G., Wang, H., Meng, H., Deng, Y., Li, J. & Gu, M. Poor Stability of Li_2CO_3 in the Solid Electrolyte Interphase of a Lithium-Metal Anode Revealed by Cryo-Electron Microscopy. *Advanced Materials* **33**, 2100404 (2021).

[32] Malmgren, S., Ciosek, K., Lindblad, R., Plogmaker, S., Kühn, J., Rensmo, H., Edström, K. & Hahlin, M. Consequences of air exposure on the lithiated graphite SEI. *Electrochimica Acta* **105**, 83–91 (2013).

[33] Wang, F., Graetz, J., Moreno, M. S., Ma, C., Wu, L., Volkov, V. & Zhu, Y. Chemical Distribution and Bonding of Lithium in Intercalated Graphite: Identification with Optimized Electron Energy Loss Spectroscopy. *ACS Nano* **5**, 1190–1197 (2011).

[34] Boniface, M., Quazuguel, L., Danet, J., Guyomard, D., Moreau, P. & Bayle-Guillemaud, P. Nanoscale Chemical Evolution of Silicon Negative Electrodes Characterized by Low-Loss STEM-EELS. *Nano Letters* **16**, 7381–7388 (2016).

[35] Holtz, M. E., Yu, Y., Gao, J., Abruña, H. D. & Muller, D. A. In Situ Electron Energy-Loss Spectroscopy in Liquids. *Microscopy and Microanalysis* **19**, 1027–1035 (2013).

[36] Lodico, J. J., Lai, C.-H., Woodall, M., Chan, H. L., Garcia, E., Hubbard, W. A., Dunn, B. & Regan, B. C. Irreversibility at macromolecular scales in the flake graphite of the lithium-ion battery anode. *Journal of Power Sources* **436**, 226841 (2019).

[37] White, E. R., Lodico, J. J. & Regan, B. C. Intercalation events visualized in single microcrystals of graphite. *Nature Communications* **8**, 1969 (2017).

[38] Kalhoff, J., Eshetu, G. G., Bresser, D. & Passerini, S. Safer Electrolytes for Lithium-Ion Batteries: State of the Art and Perspectives. *ChemSusChem* **8**, 2154–2175 (2015).

[39] Wu, H., Su, H., Joosten, R. R. M., Keizer, A. D. A., van Hazendonk, L. S., Wirix, M. J. M., Patterson, J. P., Laven, J., de With, G. & Friedrich, H. Mapping and Controlling Liquid Layer Thickness in Liquid-Phase (Scanning) Transmission Electron Microscopy. *Small Methods* **5**, 2001287 (2021).

[40] Hightower, A., Ahn, C. C., Fultz, B. & Rez, P. Electron energy-loss spectrometry on lithiated graphite. *Applied Physics Letters* **77**, 238–240 (2000).

[41] Zavadil, K. R. & Armstrong, N. R. Surface chemistries of lithium: Detailed characterization of the reactions with O_2 and H_2O using XPS, EELS, and microgravimetry. *Surface Science* **230**, 47–60 (1990).

[42] Ahn, C. C. & Krivanek, O. L. *EELS Atlas: A Reference Collection of Electron Energy Loss Spectra Covering All Stable Elements* (Gatan, 1983).

[43] Bevington, P. R. & Robinson, D. K. *Data reduction and error analysis for the physical sciences* (McGraw-Hill, Boston, 2003), 3rd edn.

[44] Arenal, R., de la Peña, F., Stéphan, O., Walls, M., Tencé, M., Loiseau, A. & Colliex, C. Extending the analysis of EELS spectrum-imaging data, from elemental to bond mapping in complex nanostructures. *Ultramicroscopy* **109**, 32–38 (2008).

[45] Cueva, P., Hovden, R., Mundy, J. A., Xin, H. L. & Muller, D. A. Data Processing for Atomic Resolution Electron Energy Loss Spectroscopy. *Microscopy and Microanalysis* **18**, 667–675 (2012).

[46] Ilett, M., S'ari, M., Freeman, H., Aslam, Z., Koniuch, N., Afzali, M., Cattle, J., Hooley, R., Roncal-Herrero, T., Collins, S. M., Hondow, N., Brown, A. & Brydson, R. Analysis of complex, beam-sensitive materials by transmission electron microscopy and associated techniques. *Philosophical Transactions of the Royal Society A: Mathematical, Physical and Engineering Sciences* **378**, 20190601 (2020).

[47] Egerton, R. F. Dose measurement in the TEM and STEM. *Ultramicroscopy* **229**, 113363 (2021).

[48] Kikkawa, J., Shiotsuki, T., Shimo, Y., Koshiya, S., Nagai, T., Nito, T. & Kimoto, K. Electron irradiation effects on lithium peroxide. *Japanese Journal of Applied Physics* **57**, 035802 (2018).

[49] White, E. R., Singer, S. B., Augustyn, V., Hubbard, W. A., Mecklenburg, M., Dunn, B. & Regan, B. C. In Situ Transmission Electron Microscopy of Lead Dendrites and Lead Ions in Aqueous Solution. *ACS Nano* **6**, 6308–6317 (2012).

[50] Malis, T., Cheng, S. C. & Egerton, R. F. EELS log-ratio technique for specimen-thickness measurement in the TEM. *Journal of Electron Microscopy Technique* **8**, 193–200 (1988).

Supplementary Materials for:

Operando spectral imaging of the lithium ion battery's solid-electrolyte interphase

Jared J. Lodico[1,2], Matthew Mecklenburg,[2,3] Ho Leung Chan,[1,2]
Yueyun Chen,[1,2] Xin Yi Ling,[1] and B. C. Regan[1,2]

[1] *Department of Physics and Astronomy, University of California, Los Angeles, CA 90095, U.S.A*
[2] *California NanoSystems Institute, University of California, Los Angeles, CA 90095, U.S.A*
[3] *Core Center of Excellence in Nano Imaging, University of Southern California, Los Angeles, CA, 90089, U.S.A*

Contents

Tables

Figures

SM

SM.1 Imaging Parameters Summary

	Figs. 2–3		Fig. 4		
	surveying	low-loss	surveying	low-loss	core-loss
beam current (pA)	75	75	300	300	300
dwell time (ms)	0.019	48	0.19	35	100
pixel size (nm)	9.8	21	16	11.1	30.3
probe size (nm)	0.7	0.7	1.5	1.5	1.5
pixel/probe area ratio	250	1200	150	70	520
pixel fluence ($e/\text{Å}^2$)	1	490	14	5300	2000
probe fluence ($e/\text{Å}^2$)	230	580,000	2000	370,000	1,100,000
image size (pixels)	1024×1024	240×120	512×512	125×511	50×50
dispersion (eV/bin)	n.a.	0.05	n.a.	0.05	1
full bandwidth (eV)	n.a.	102.4	n.a.	102.4	11 to 2059
vertical binning	n.a.	5	n.a.	10	1
GIF aperture (mm)	2.5	2.5	2.5	2.5	5

Table S1: Imaging parameters. To ensure that the 'low-loss' spectra capture the entire zero-loss peak, we acquire an energy range of roughly -10 to 90 eV in those datasets. We write 'low-loss' because these spectra also capture the Li core-loss signal near 55 eV, which is at a particularly low energy due to lithium's small atomic number $Z = 3$ [42]. The 'core-loss' spectrum image that is acquired after the Fig. 4 low-loss spectrum image spans 11–2059 eV, which covers the carbon, nitrogen, and oxygen K-edges. This spectrum image is discussed in Figs S9–S12.

SM.2 Movie captions

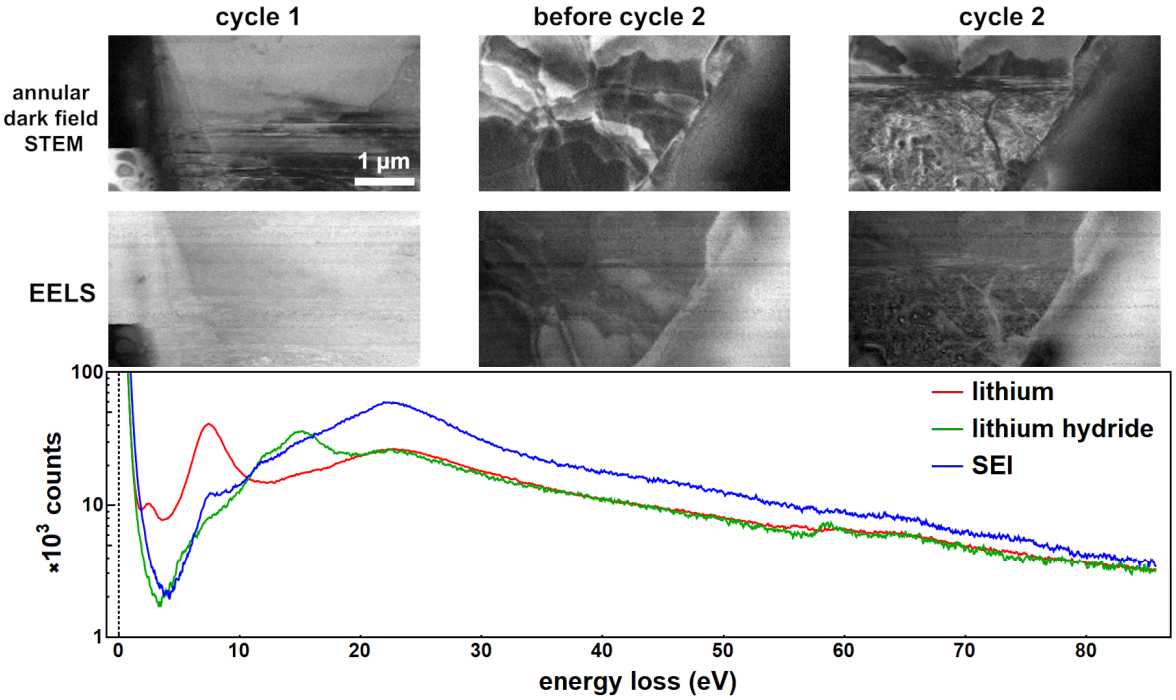

Movie S1: **Spectrum images of first lithiation, delithiated graphite, and second lithiation.** This movie combines the data from the three spectrum images that are featured in Fig. 2 and Fig. 3. ADF images (top row), energy filtered images (second row, 50 meV bandwidth), and the full spectra for several reference materials (bottom, see Fig. 2) are shown together. The particular energy slice shown in the energy filtered image is indicated by the dotted line on the bottom plot. The frame shown in the still figure above this caption highlights the LiH signal, which appears strongly in dendrites in the lower left of the cycle 1 field of view and in the lower right of the cycle 2 field of view. To best explore the data set, a movie player with a status bar that can be dragged to highlight various energy windows of interest is recommended for viewing.

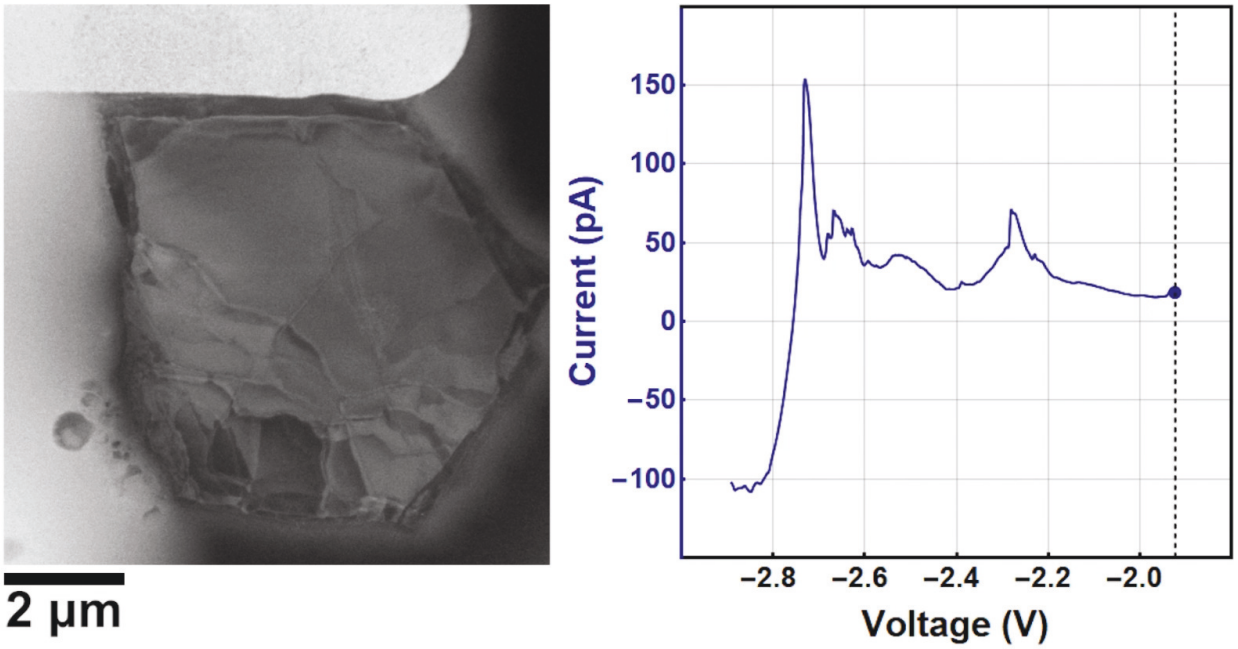

Movie S2: **Annular dark field imaging of first delithiation.** ADF STEM images of a graphite flake (left) in the process of delithiating are synchronized with the cyclic voltammogram (CV) (right). Here the potential is ramped at a constant rate of 2 mV/s. The 1024 × 1024 pixel ADF STEM images that constitute the movie are acquired with manual timing at an approximate rate of one frame per 30 s, where the frame acquisition time is 20 s and the time required to save each image is approximately 10 s. The video plays the 15 ADF images at a rate of 1 frame per second. To see the relatively small effect of imaging vs. lithiation/delithiation on this sample, see also Fig. 1 and Movie S3.

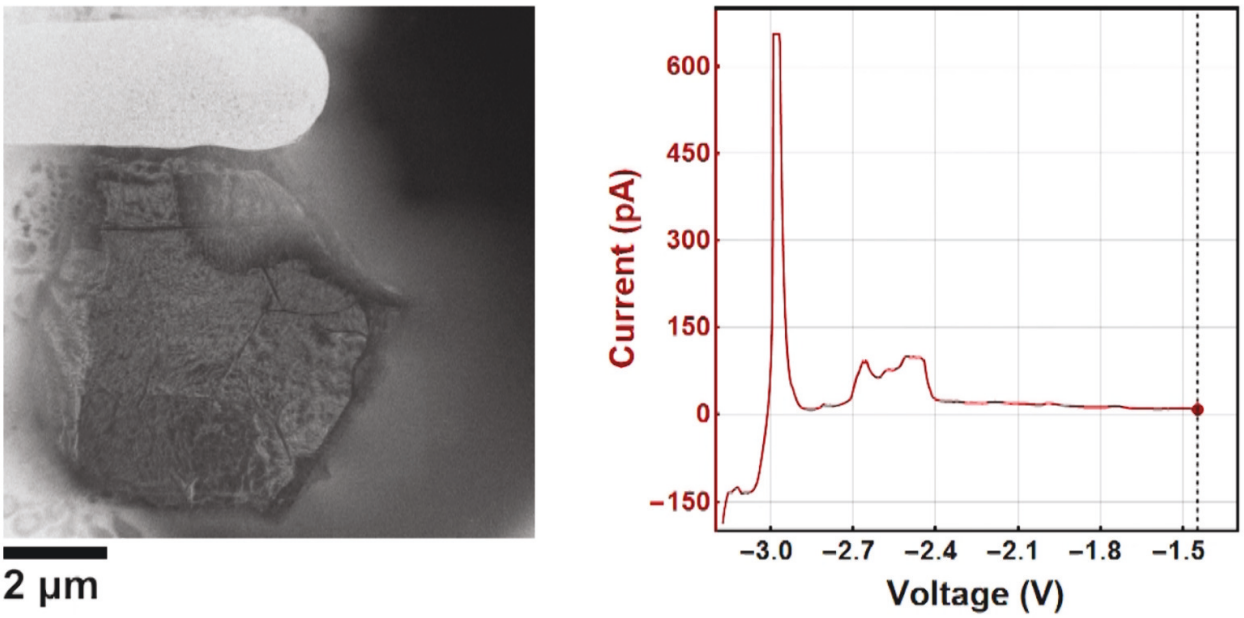

Movie S3: **Annular dark field imaging of second delithiation.** ADF STEM images of a graphite flake (left) in the process of delithiating are synchronized with the cyclic voltammogram (CV) (right). Here the potential is ramped at a constant rate of 2 mV/s. The first seventeen 1024×1024 pixel ADF STEM images (21 images in total constitute the movie) are acquired with manual timing at an approximate rate of one frame per 30 s, where the frame acquisition time is 20 s and the time required to save each image is approximately 10 s. The delays between the last four ADF images are longer (up to several minutes). To see the relatively small effect of imaging vs. lithiation/delithiation on this sample, see also Fig. 1 and Movie S2.

In this movie, and perhaps in Movie S2, some motion of the electrolyte is evident. This motion has little effect on the measured current (see particularly the time $t > 10$ s in this movie), which highlights another advantage of capping the electrodes with ALD alumina. The working electrode is immersed where it is bare, except perhaps over some small regions of graphite shown (the Pt current collector for the working electrode is covered with ALD alumina). Thus, electrolyte motion is not producing sizable electrical currents. The measured electrical currents are due to chemistry (intercalation, dendrite growth, SEI formation, etc.), as desired.

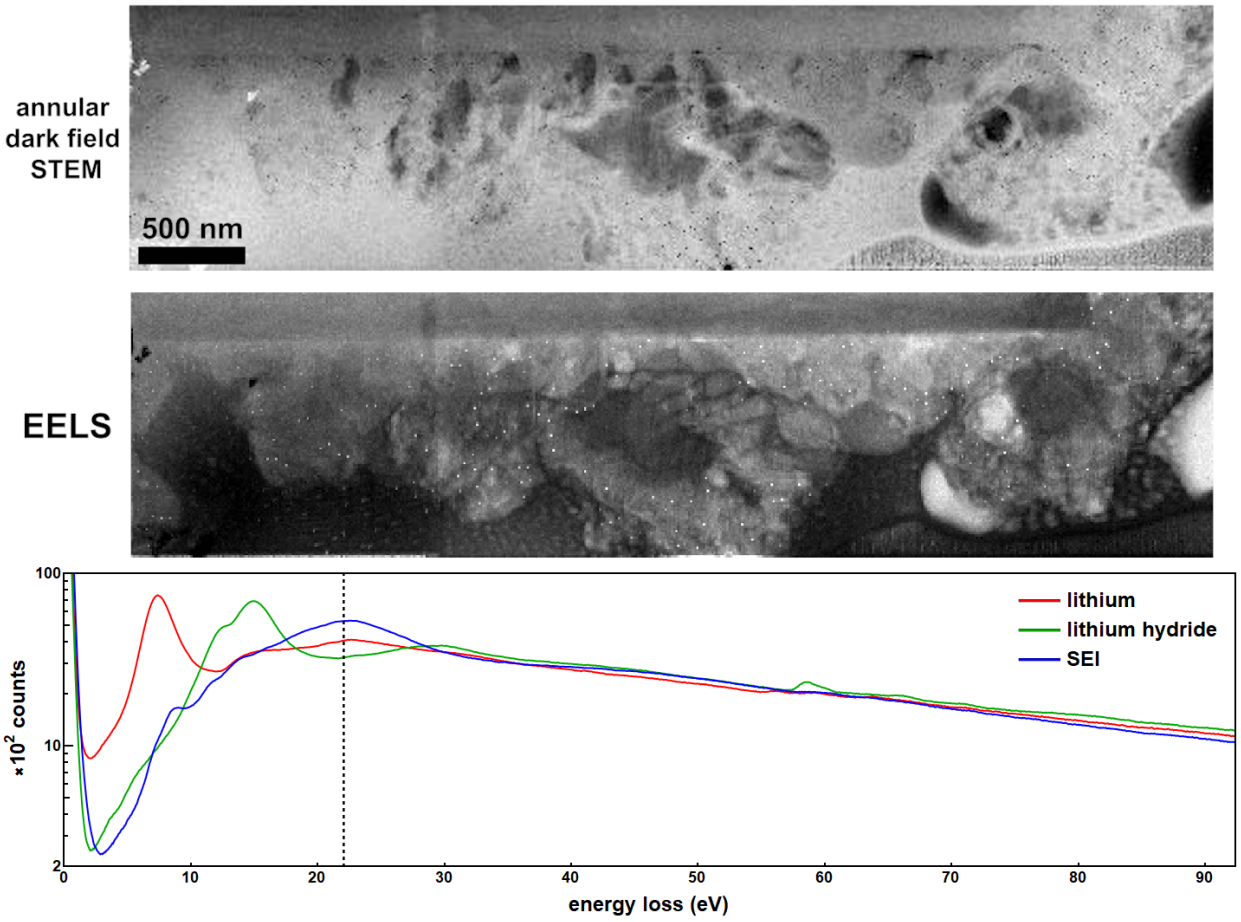

Movie S4: **Spectrum image of well-developed SEI.** This movie summarizes the spectrum image used to generate Figs. 4B–E and Fig. S8. The ADF STEM image shown on top is acquired simultaneously with the spectrum image. As with Movie S1, the scanning dotted line indicates the 50 meV energy slice shown in the EELS image. (Again, a movie player with a status bar that can be dragged to highlight various energy windows of interest is recommended for viewing.) The ADF image shows some changes from the previously acquired survey image (Fig. 4A). For example, a dark region at the far right, most likely a gas bubble, has evolved. Other signs of beam damage include the single-pixel-size spots in the spectrum image that are brighter than their surroundings at low energy and darker at high energy. We attribute these spots to chance overlap between the exact beam position and a location damaged by the beam previously (recall that the probe size is much smaller than the pixel size — see Table S1) during survey imaging. These spots appear only in the SEI and appear more frequently with repeated imaging, highlighting the particular sensitivity of the SEI to beam damage.

SM.3 Supplementary Figures

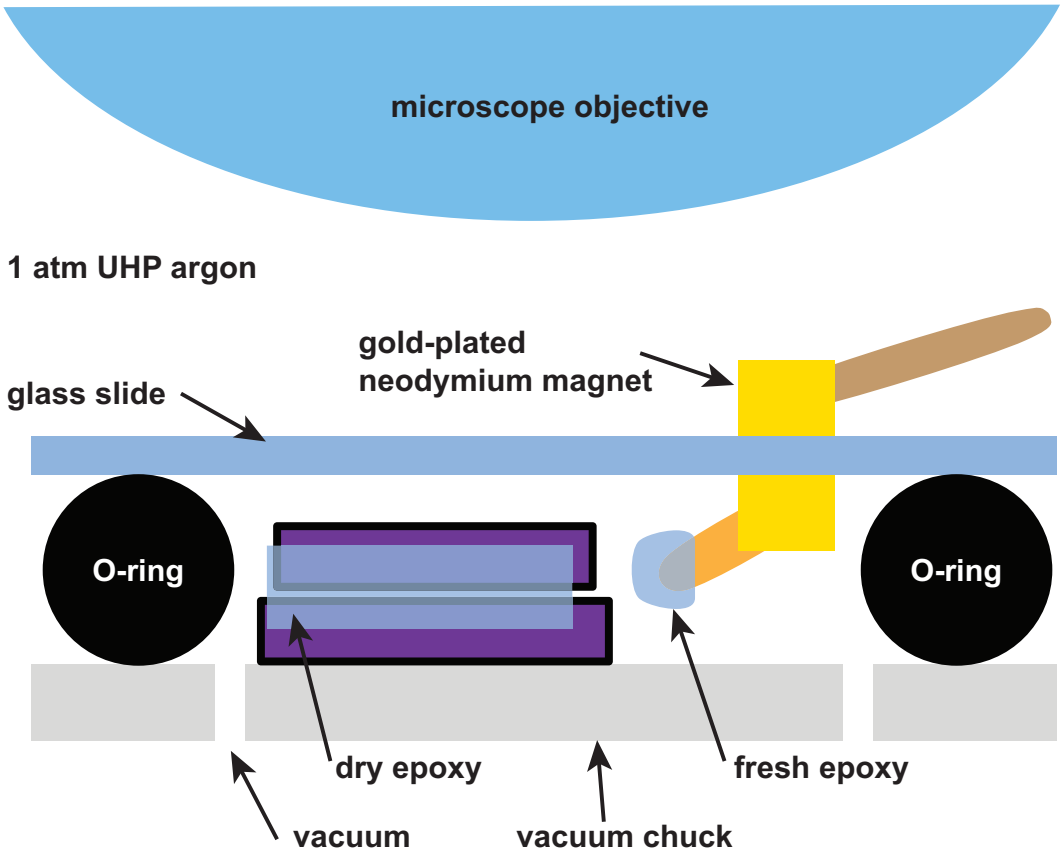

Figure S1: **Fluid cell assembly diagram.** The final steps of the cell assembly take place in a custom-made glove bag under an argon atmosphere. Inside the bag, three sides of the cell are epoxied together using the micromanipulators in a probe station equipped with an optical microscope. The fourth and final side is epoxied under vacuum (see Fig. 1 and Methods). The small, easily assembled vacuum chamber sits under the microscope objective and consists of a custom vacuum chuck, an O-ring, and a glass slide as shown (not to scale). Mechanical access for applying the epoxy is provided by a pair of 2-mm cube NdFeB magnets that transmit forces applied to the magnet outside the chamber, through the glass, to the magnet inside the chamber. The magnets slide freely on the glass, allowing the operator to apply the final, sealing coat of epoxy under vacuum, and thus to create a fluid cell that will remain thin in the TEM vacuum.

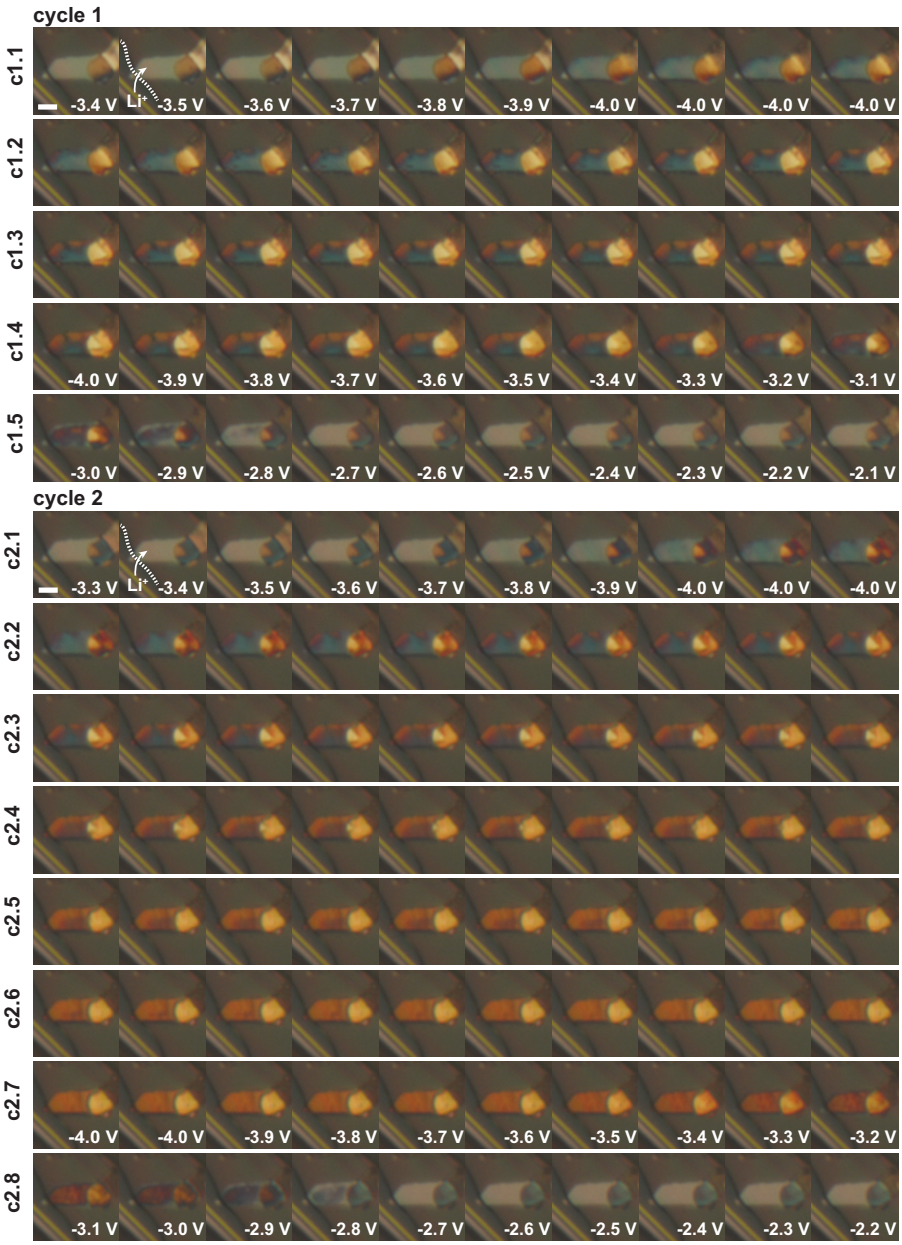

Figure S2: **Optical view of graphite lithiation/delithiation in a TEM fluid cell.** A TEM fluid cell, assembled as described in Methods, is imaged optically [36] over two sequential lithiation/delithiation cycles. The image acquisition times are separated by 10 s, so each row represents a a time span of 100 s. The potential ramp rates are ± 10 mV/s between the open circuit potential (OCP) of −0.5 V vs. Pt and −4.0 V vs. Pt, and the potential is held at −4.0 V for 250 s and 540 s after the first and second lithiations, respectively. The scale bars shown are 3 μm. The graphite's color changes [36] from gray to gold and back demonstrate full lithiation (to LiC_6) and delithiation in the TEM electrochemical fluid cell. Two frames with Li^+ labels highlight the boundary of the electrolyte; the left tip of the flake is immersed, while the remainder on the right is dry.

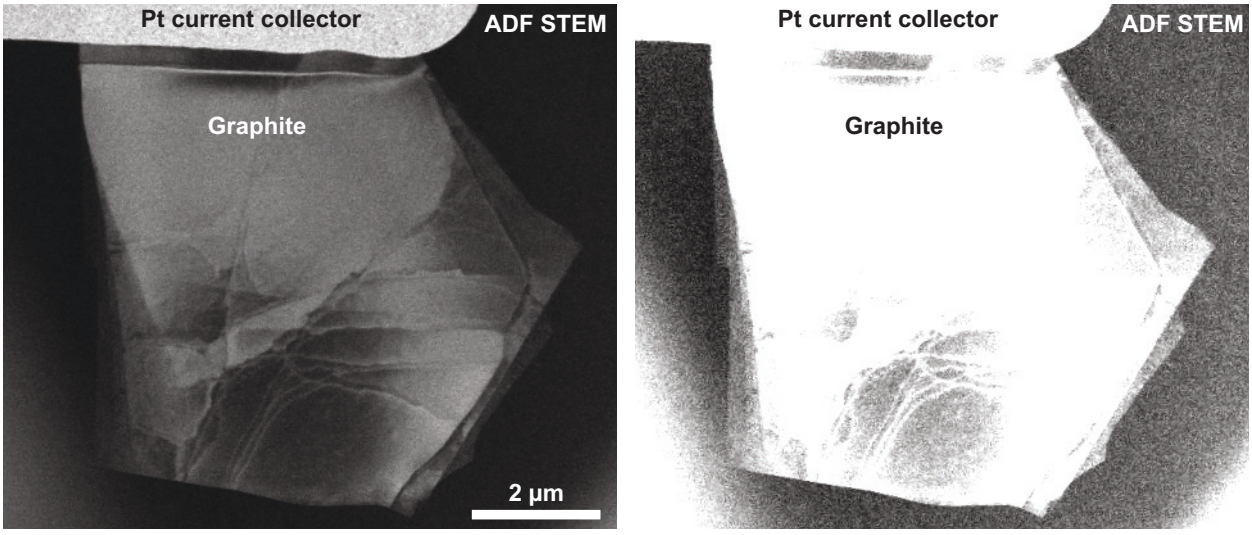

Figure S3: **Graphite edge determination.** (left) Lower magnification ADF STEM image of the graphite flake in Figs. 1, 2, and 3, shown with typical contrast and brightness values. (right) Adjusting the contrast and brightness of the left image makes the true edges of the graphite flake visible.

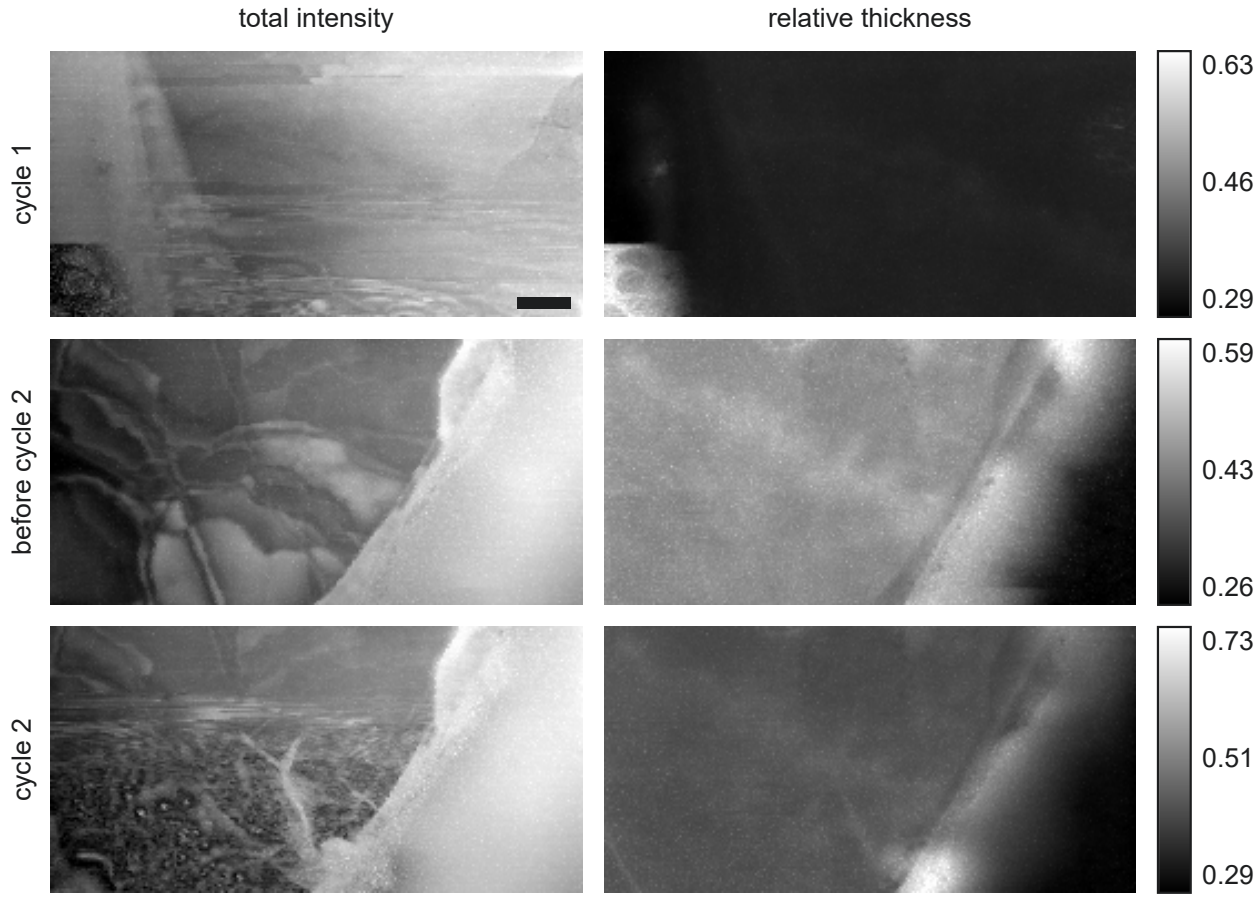

Figure S4: **EELS thickness maps, first sample.** These six images are constructed from the spectrum images used to generate Figs. 2–3. Created by integrating over the entire energy spectrum, the images in the left column give a 'bright field' representation of the sample, illustrating its structural evolution during cycle 1 and 2, and its (static) structure between the cycles. In the right column, the relative thickness maps are created using the 'log-ratio' method [50]. The intensity scale bars describe the dimensionless thickness ratio t/λ, where t is the sample thickness and λ is the electron mean free path (mfp). For the imaging conditions used, the following materials have an estimated [50] mfp, given in parentheses, of: lithium (200 nm), lithium hydride (220 nm), graphite (160 nm), Li_2CO_3 (160 nm), EC:DMC (180 nm), and silicon nitride (140 nm). These mfp numbers, especially those of the compounds, are to be considered rough, as they are derived assuming standard elemental densities. By themselves, the two 20-nm-thick Si_3N_4 membrane windows separating the fluid cell interior from the TEM vacuum represent a t/λ of 0.29, within 10% of the minimum total thickness measured. Taking a mfp of 200 nm to be characteristic of the other materials, we see that the non-window material varies from near zero to 70-, 60-, and 90-nm-thick for the cycle 1, before cycle 2, and cycle 2 spectrum images respectively. Interestingly, the cell thickness varies both in space and in time. For these spectrum images a $t/\lambda \sim 0.5$ is typical, which corresponds to 40 nm of Si_3N_4 and 30–50 nm of LIB material.

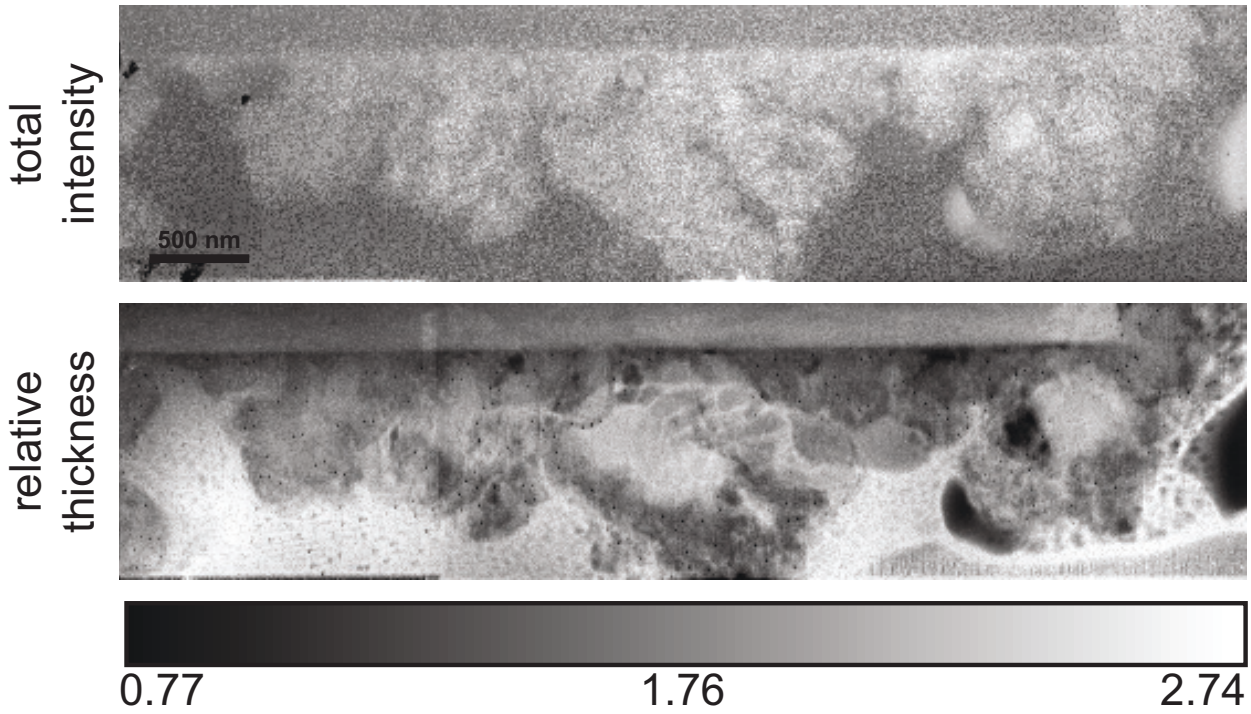

Figure S5: **EELS thickness map, second sample.** These two images are constructed from the spectrum image used to generate Fig. 4 using the methods of Fig. S4. This sample is thicker than the first: t/λ varies from 0.8 to 2.7, of which 0.5 to 2.4 can be attributed to the contents of the fluid cell. Again taking a mfp of 200 nm to be characteristic of the LIB materials, we see that the non-window material varies from 100 to 500-nm thick. Unlike the ADF STEM image (Fig. 4A), which captures electrons scattered to angles 20–40 mrad and highlights the Li and LiH dendrites within the SEI, the total intensity image highlights the SEI and dendrites uniformly. The relative thickness image shows the dendrites to have larger t/λ relative to the rest of the SEI.

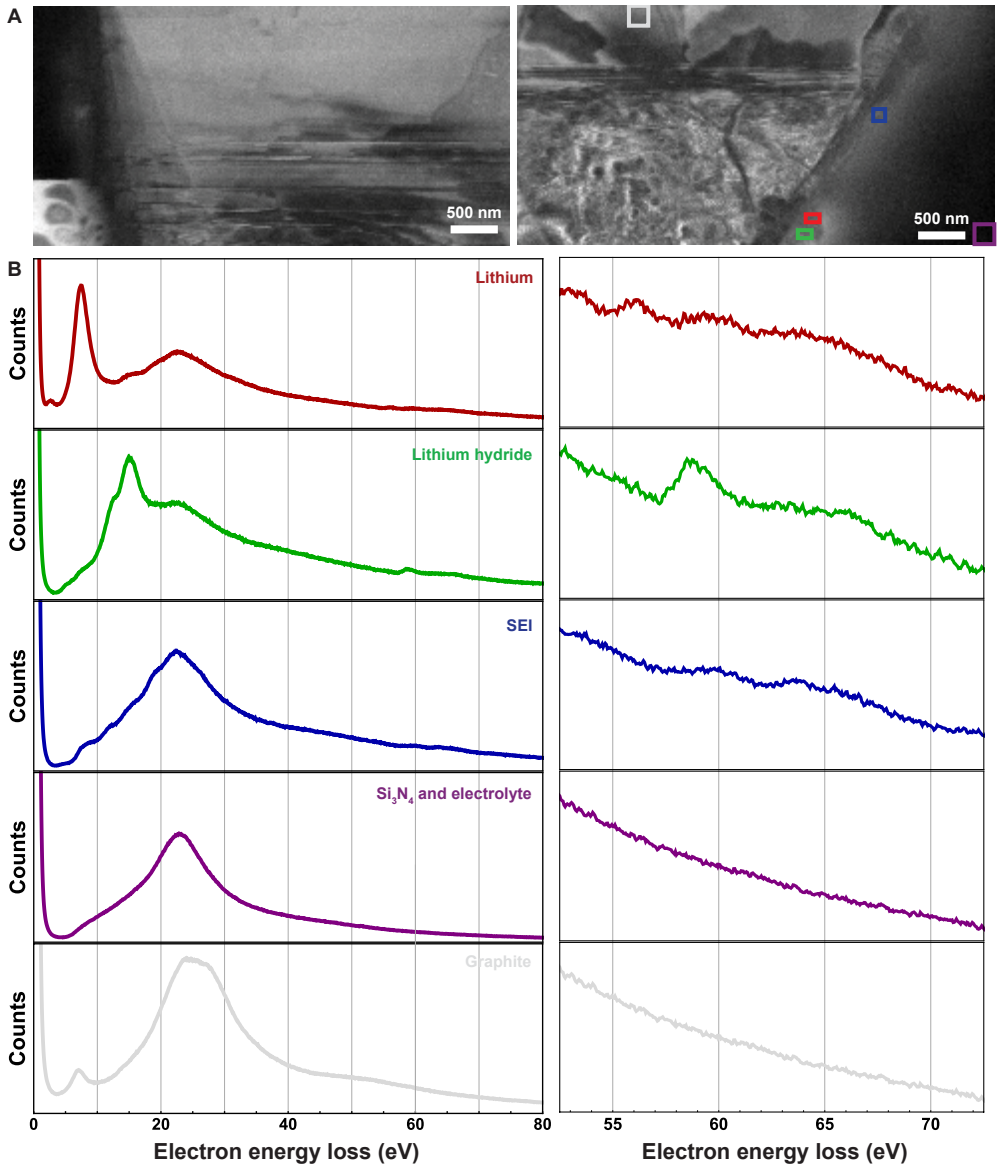

Figure S6: **Multiple linear least-squares (MLLS) fitting reference spectra for Fig. 2. (A)** The left and right ADF images show the data of Fig. 2B and Fig. 2E, respectively. Colored boxes in the right ADF image indicate regions that, due to their location and morphological and spectral uniformity, can be considered to be representative of a given material. **(B)** Representative spectra for Li, LiH, the SEI, the Si_3N_4 & electrolyte, and the graphite, as determined by averaging the acquired spectra across the regions framed by correspondingly colored rectangular boxes in part (A). No subtractions are performed. For instance, the 'graphite' spectrum also includes a contribution from the Si_3N_4 membrane window, which spans the entire field of view. MLLS fitting is applied over the energy range 4–40 eV. Li K-edge signals (right plots, which are zoom views of the left plots) show evidence of Li in the lithium, the lithium hydride, and the SEI, but not in the other materials, as expected.

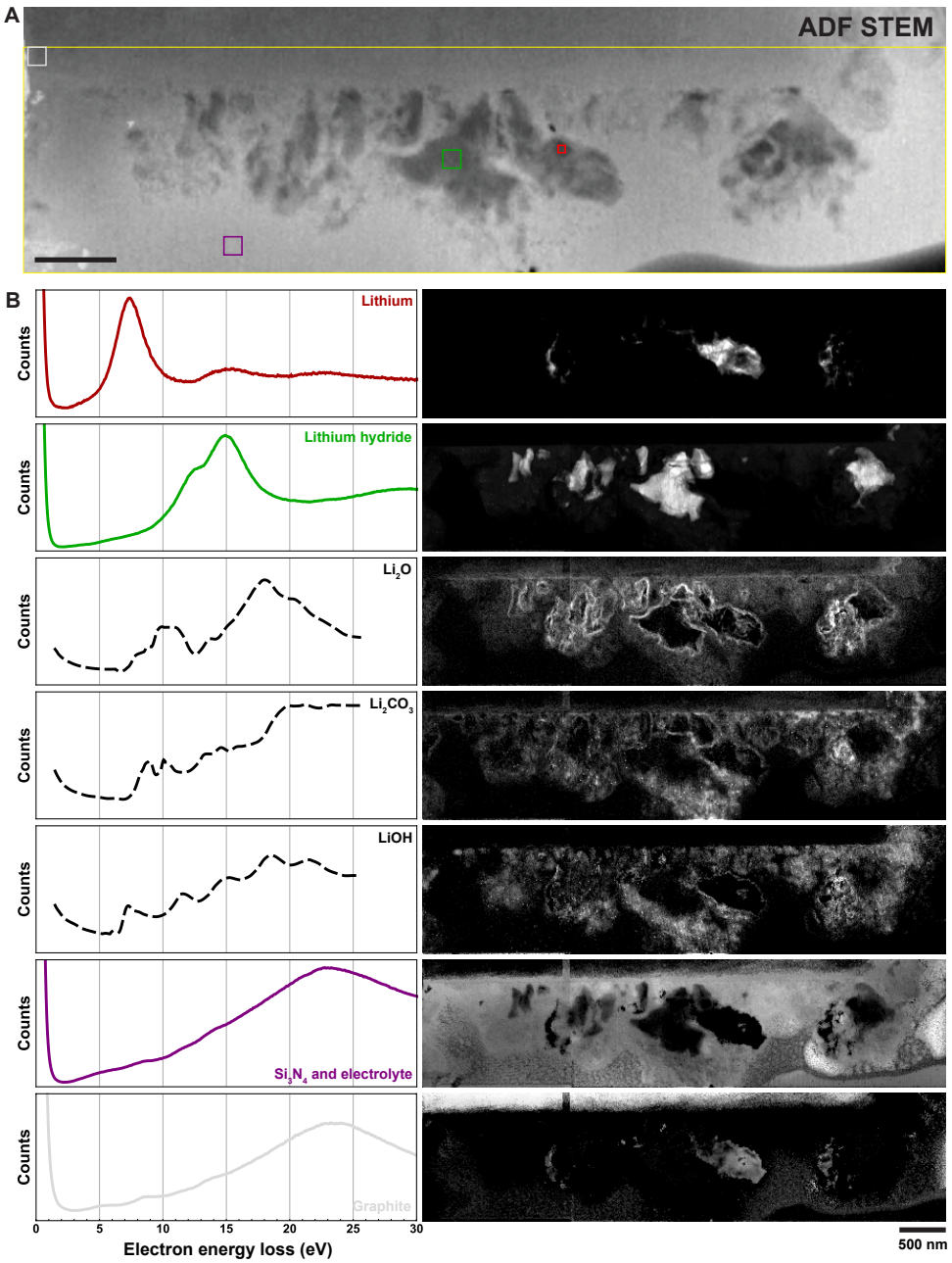

Figure S7: **Multiple linear least-squares (MLLS) fitting reference spectra and component maps for Fig. 4.** On the ADF survey image **(A)**, a reproduction of Fig. 4A, rectangular boxes indicate the spectrum image field of view (yellow) and the locations chosen to produce representative spectra **(B)** of Li (red), LiH (green), the Si_3N_4 membrane window and electrolyte (purple), and the graphite (gray). As described previously (Fig. S6), no subtractions are performed. Although the ZLP is shown in the spectra acquired in this spectrum image (the others are from [48]), only the window 5–25 eV is used for fitting.

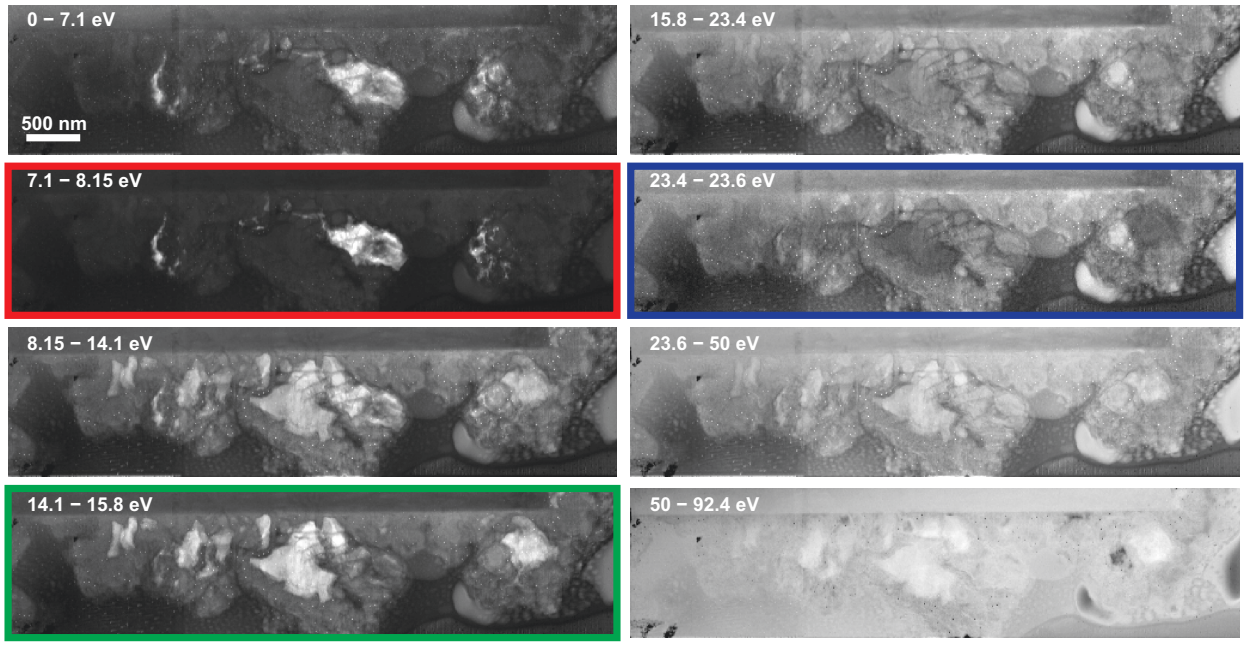

Figure S8: **Energy segmented spectrum image of a well developed SEI.** To give a still rendition of Movie S4, the source spectrum image is segmented into 8 different energy slices, each of which corresponds to the signal integrated over the indicated energy bandwidth. The bandwidths vary from slice to slice. The frames with the red, green, and blue colored outlines show energy windows that indicate roughly the spatial distribution of the Li, LiH, and the SEI, respectively. This crude segmented display corroborates the more sophisticated MLLS approach presented in Fig. 4 of the main text.

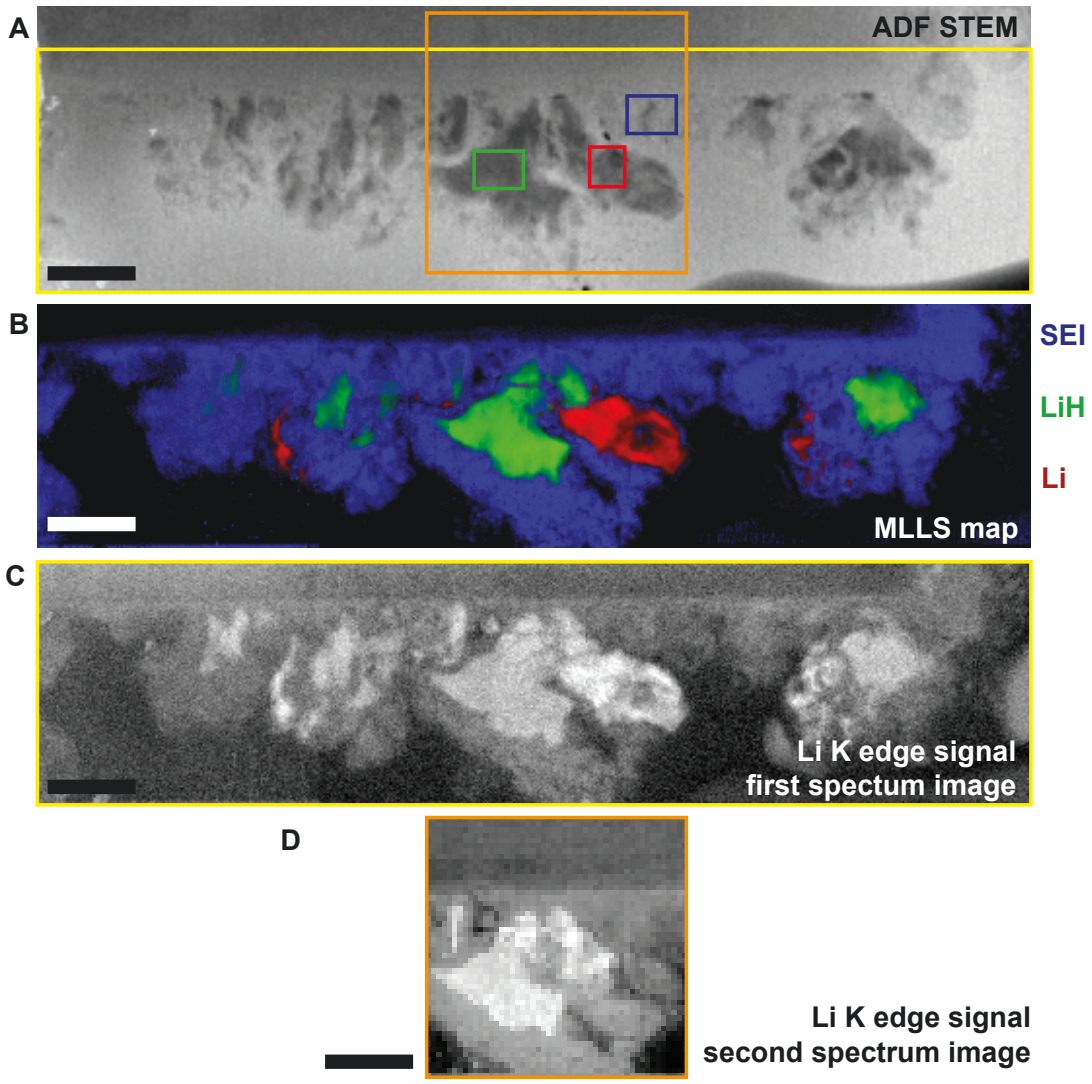

Figure S9: **Li spectrum imaging, map summary.** The ADF image **(A)**, a reproduction of Fig. 4A, shows the sample before any spectrum imaging. The orange box indicates the field of view of the second, 'core-loss' spectrum image of the same sample (Table S1). The MLLS map **(B)** shows the spatial distribution of the lithium, the lithium hydride, and the SEI, as determined by fits to the low-loss portion of the first spectrum image using reference spectra acquired from the indicated regions. At a given pixel, integrating the individual background-subtracted core-loss intensities provides an indication of the quantity of corresponding element at that location. Applying this algorithm, which is described in detail in the caption of Fig. S11, to the Li K-edge signal produces **(C)** and **(D)** from the first (102.4 eV bandwidth) and second (2048 eV bandwidth) spectrum images, respectively. [The map (D) is a reproduction of Fig. S11C.] Relative to the Li K-edge signal in the lithium hydride dendrite, the Li K-edge signal in the lithium dendrite goes from being more intense in (C) to less intense in (D). Thus the lithium appears to be less stable than the lithium hydride under these (room temperature liquid cell) imaging conditions. The scale bars are 500 nm.

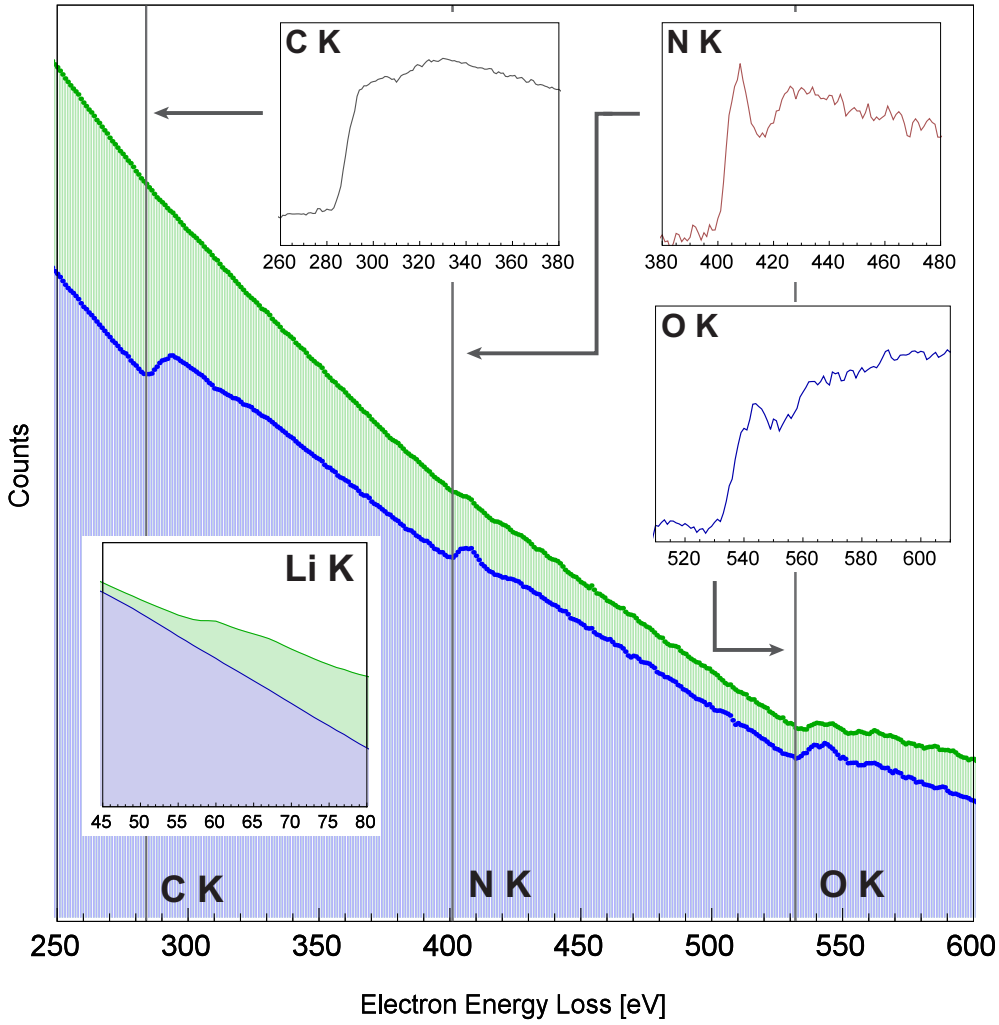

Figure S10: **2048 eV bandwidth spectrum image, spectra.** Average spectra collected from the correspondingly colored green and blue rectangles in the 11–2059 eV bandwidth spectrum image (Fig. S9). The insets show the Li K-edge (lower left), and the background-subtracted C, N, and O K-edges from the SEI (upper right), respectively, all from the same spectrum. K-edge resonances at 284 and 532 eV reveal the presence of carbon and oxygen, respectively, in the SEI. The nitrogen core-loss signal at 402 eV we attribute to the silicon nitride membrane windows. With this larger bandwidth the Li K-edge is still visible in the lithium hydride, but not in the SEI. The observed carbon and oxygen K-edge structure in the SEI is consistent with lithium carbonate and lithium semi-carbonates (i.e. alkyl carbonates) [8, 10, 30, 34], but the signal-to-noise ratio and the confounding effects of the electrolyte background together prevent the stoichiometry or chemical bonding states from being quantified precisely (Fig. S11).

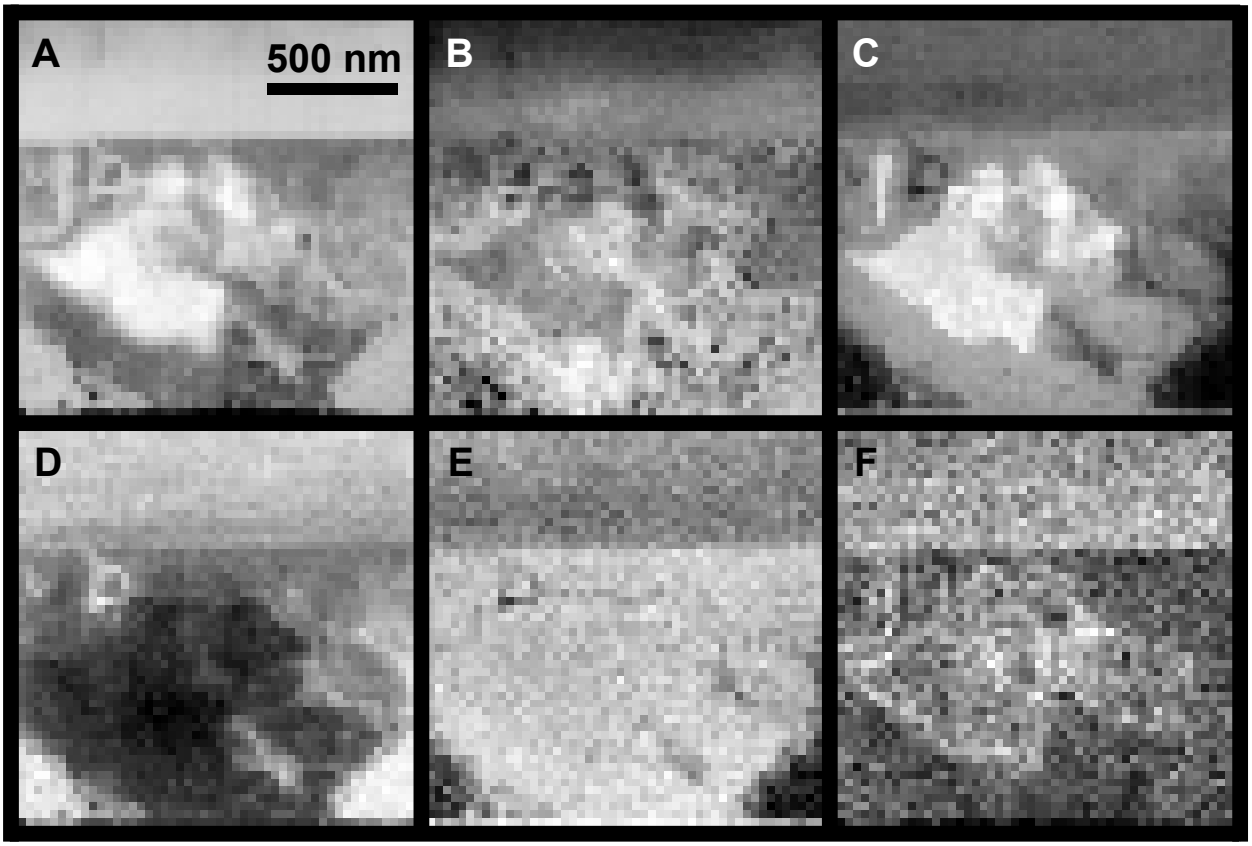

Figure S11: **2048 eV bandwidth spectrum image, maps.** **(A)** Total intensity/virtual bright field formed by integrating the intensity over the entire 2048 eV bandwidth of the 'core-loss' spectrum image (Fig. S9, Table S1). **(B)** Annular dark field image acquired simultaneously. **(C)** Lithium signal after the Li K-edge at 55 eV, **(D)** carbon signal after the C K-edge at 284 eV, **(E)** nitrogen signal after the N K-edge at 402 eV, and **(F)** oxygen signal after the O K-edge at 532 eV. To extract the Li core-loss signal (C) we subtract an exponential background determined in a 20 eV bandwidth immediately below the edge, and integrate the remaining signal in a 11 eV bandwidth after the edge. To extract the C, N, and O core-loss signals (D,E,F), we subtract a power-law background determined in a 70 eV bandwidth 5–10 eV before the corresponding edge, and integrate the remaining signal in a 105 eV bandwidth after the edge. The lithium hydride dendrites show a significantly stronger Li signal than the lithium metal and some indication of an oxide shell [30]. The graphite is clearly visible at the top of all four (unnormalized) K-edge maps. Its presence in the nitrogen map, which might otherwise be expected to show a flat field, indicates that the K-edge intensities cannot be simply interpreted as proportional to the number of atoms of the corresponding element present.

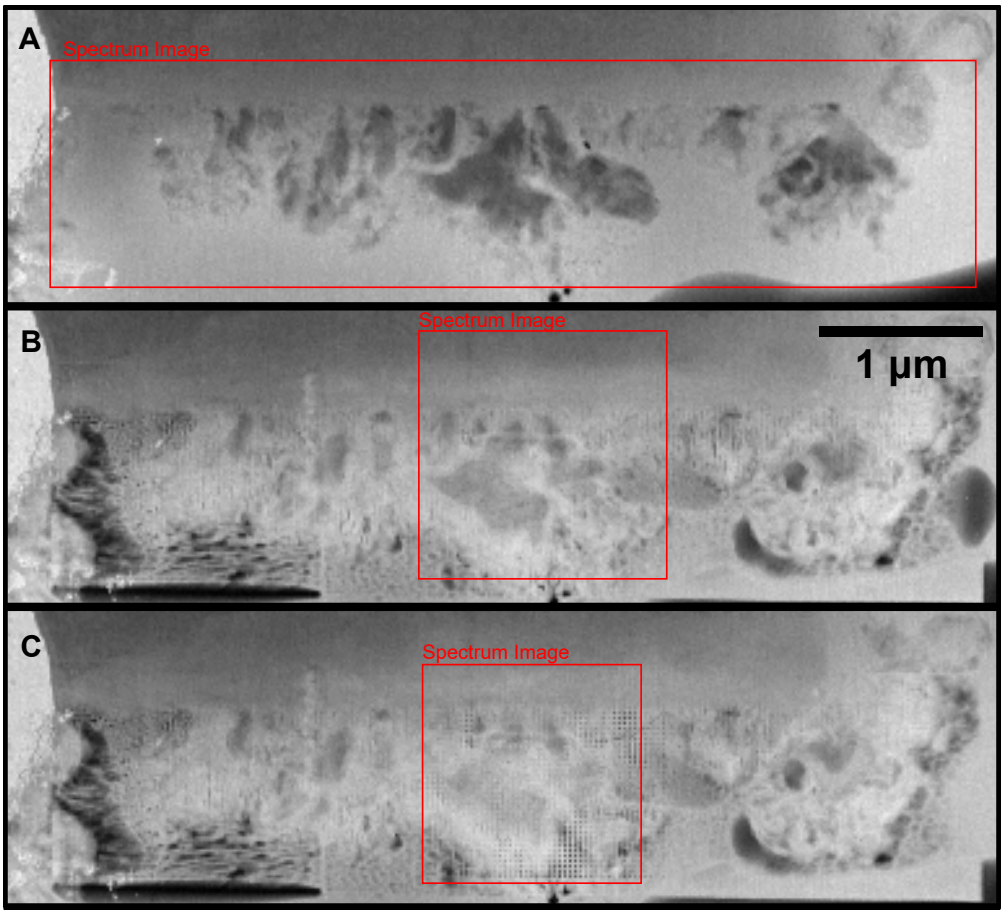

Figure S12: **Dose effects in survey images.** Survey images acquired *before* the **(A)** first, **(B)** second, and **(C)** third spectrum images of the Fig. 4 sample. Acquiring the first spectrum image damages the pristine SEI (A), as evidenced by the decreased contrast difference between the Li and LiH dendrites and their surroundings (B). The second spectrum image, with its 10× longer dwell times (Table S1), imprints a visible grid of damage (C) in the SEI, but not elsewhere. Because the SEI is so obviously compromised after the second spectrum image, no data from the third spectrum image are presented in this paper.

Improving the signal-to-noise ratio for spectroscopy of the SEI represents a major challenge, as the carbon-containing components of the SEI are more beam sensitive than the other cell components (i.e. the Li, the LiH, the graphite electrode, and the electrolyte) [31,33]. This sensitivity is evident in the first spectrum image (Movie S4), which shows single pixel spots that are noticeably brighter than their surroundings below 40 eV. We attribute these spots to chance overlap of the beam with a region previously damaged during survey imaging. They appear only in the SEI, and become more common with repeated imaging. Spectrum imaging, with its characteristically longer dwell times, makes the damage obvious even to ADF imaging by imprinting an array in the SEI that reflects the mismatch between the probe size and the pixel size (Table. S1). We conclude that, in its native, room-temperature liquid electrolyte, even comparatively low-dose survey imaging damages the SEI, and that the ability of any spectrum to faithfully reflect the SEI's constituent compounds in the unimaged, pristine state must be critically considered in light of the total dose delivered.